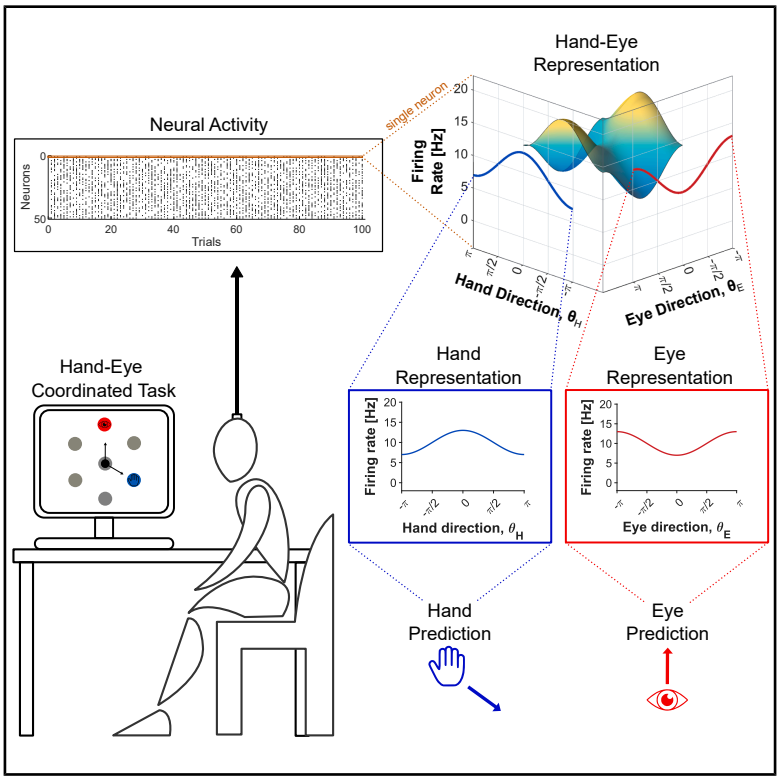
Report

Cell Reports

The compositional encoding of hand-eye coordinated movements for single neurons in the posterior parietal cortex

Graphical abstract



Highlights

- Human posterior parietal neurons exhibit mixed hand-eye selectivity
- Mixed-selective representations are additively separable into hand and eye codes
- Hand and eye codes generalize across single- and multi-effector contexts
- Compositional coding enables modular decoding of coordinated movements

Authors

Nikos A. Mynhier, Jorge Gamez, Kellan P. Moorse, Kelsie Pejsa, Ausaf Bari, Richard M. Murray, Richard A. Andersen

Correspondence

nmynhier@caltech.edu (N.A.M.), richard.andersen@vis.caltech.edu (R.A.A.)

In brief

Some brain regions are theorized to represent complex behaviors through compositions of simpler neural building blocks. Mynhier et al. provide an example, showing that hand and eye movements are compositionally encoded in human posterior parietal cortex, providing a framework for modular neural decoding.

Mynhier et al., 2026, Cell Reports *45*, 118204
November 24, 2026 © 2026 The Authors. Published by Elsevier Inc.
https://doi.org/10.1016/j.celrep.2026.118204

CellPress

Cell Reports

CellPress
OPEN ACCESS

Report

The compositional encoding of hand-eye coordinated movements for single neurons in the posterior parietal cortex

Nikos A. Mynhier,[1,5,*] Jorge Gamez,[1] Kellan P. Moorse,[1] Kelsie Pejsa,[1] Ausaf Bari,[3,4] Richard M. Murray,[1,2,4] and Richard A. Andersen[1,4,*]

[1]Division of Biology and Biological Engineering, California Institute of Technology, Pasadena, CA 91125, USA
[2]Division of Engineering and Applied Science, California Institute of Technology, Pasadena, CA 91125, USA
[3]Department of Neurosurgery, David Geffen School of Medicine at UCLA, Los Angeles, CA 90095, USA
[4]Senior author
[5]Lead contact
*Correspondence: nmynhier@caltech.edu (N.A.M.), richard.andersen@vis.caltech.edu (R.A.A.)
https://doi.org/10.1016/j.celrep.2026.118204

SUMMARY

Human posterior parietal cortex (PPC) is known to play a role in hand-eye (H-E) coordination, yet the underlying encoding mechanisms remain uncertain. We recorded 412 single neurons across 11 sessions from motor cortex (MC; n = 251) and PPC (n = 161) in a single human participant performing an H-E coordinated center-out task. While MC neurons showed negligible modulation by eye movements, 79% of PPC neurons had neural representations that were additively separable into independent hand- and eye-movement tuning curves. Due to this separability, representations could be separated and additively recomposed while maintaining structural similarity. Consequently, compositional decoders trained solely on single-effector movements could match the performance of decoders trained on coordinated H-E movements (hand: 66% vs. 69%; eye: 34% vs. 36%). These results show that, during simple center-out tasks, MC hand-movement codes are unaffected by eye movements and that compositionality can be used to modularly decode H-E coordinated movements in PPC.

INTRODUCTION

The human posterior parietal cortex (PPC) is a core part of the dorsal visual stream, a processing pathway that governs how vision is used for physical actions.[1] In particular, PPC encodes spatial processing for visually guided actions[2–4] and supports effective hand-eye (H-E) coordination during natural behaviors, including reaching and grasping.[5–7] The encoding of H-E coordination in PPC has been studied extensively in nonhuman primate (NHP) models, across diverse experimental paradigms.[5–25] Throughout these studies in NHPs, PPC has proved to be a heterogeneous region with many different areas and functional properties.[26–30] While many NHP findings remain unverified in humans, human lesion studies indirectly confirm PPC's critical role in H-E coordination.[31,32] For example, damage to PPC can result in optic ataxia, a disorder impairing visually guided reaching despite intact primary visual and motor function. Patients with optic ataxia often misreach for targets, particularly in peripheral vision or contralesional space, consistent with a disruption in transforming visual information into appropriate motor commands.[31] PPC lesions can also produce spatial neglect syndromes, in which movements toward one side of space are systematically impaired.[33] Together, these deficits indicate that the link between vision and action is fundamentally compromised following PPC damage.

Hand and eye movements performed separately have previously been decoded from PPC in brain-machine interface (BMI) studies.[34,35] However, the decoding of simultaneous hand and eye movements has yet to be explored systematically with BMIs. Decoding coordinated H-E movements is particularly important because they commonly arise in BMI settings due to gaze shifts accompanying nearly all natural motor behaviors.[36] Although, the best way to decode simultaneous H-E movements is still unknown.

In recent years, BMI studies in the motor cortex (MC) have increasingly observed the neural representations of multi-variable motor movements, such as multi-limb, multi-finger, and bimanual movements, to be compositional.[37–42] A neural representation is considered compositional when it can be separated into independent codes corresponding to each variable of a movement. Such a structure has enabled the construction of complex BMIs which require multiple degrees of freedom, such as writing or piloting cars and drones.[43–45] While motor movements appear to be compositional, it is unclear whether visual signals can also be composed with motor signals during H-E coordination. Moreover, while compositionality has been shown

This is an open access article under the CC BY license (http://creativecommons.org/licenses/by/4.0/).

in PPC,[46,47] most compositional BMIs rely on MC. Thus, here we test whether H-E representations in PPC exhibit the compositional structure and can support compositional decoding.

To test compositionality, we characterize single-neuron representations of H-E coordinated movements in the hand knob of MC and the superior parietal lobule (SPL) of PPC during a standard center-out task. We find that mixed selective neurons have additively separable codes for hand and eye movements. We also find that univariate (or single-effector [SE]) representations of isolated hand or eye movements generalize to multi-effector (ME) representations of coordinated H-E movements. Crucially, these properties allow us to create compositional decoders. We demonstrate that compositional decoders trained solely on SE data can predict coordinated H-E movements as well as decoders trained directly on ME data. Together, these findings support that, in common BMI contexts, H-E representations in human SPL can be treated as compositional and support scalable, efficient decoding.

RESULTS

Single neurons have composable and separable hand-eye representations

We performed an H-E coordination task (Video S1) with two kinds of trials, SE and ME, across 11 clinical sessions. Both kinds of trials use a 6-target, center-out structure. During an ME trial (Figure 1A), both a hand reach and gaze shift are made simultaneously toward targets presented at angles θ_H and θ_E. During the SE trials (Figure 1D), only one movement (hand or eye) is made toward a single presented target with the other effector fixed. Trial type was indicated by the target configuration, with no separate instructional cue period. ME trials presented two perimeter targets, whereas SE trials presented one perimeter target and one target at the center fixation position. A block of trials comprised 3 repetitions of all 49 trial types (36 ME, 12 SE, and 1 control), presented in a pseudo-random order. Over the course of a clinical session, 2–3 blocks were completed (see STAR Methods).

SE trials provided a controlled characterization of how movements of each effector independently modulated neuronal firing rate (FR). The resulting hand and eye tuning curves (TCs), $f_H^{SE}(\theta_H)$ and $f_E^{SE}(\theta_E)$, respectively (Figure 1E), were 6×1 vectors representing an example SPL neuron's mean FR at each of the six discrete target angles (see STAR Methods). ME trials helped to characterize how simultaneous hand and eye movements modulated neuronal FR. For the same example neuron, the resulting joint H-E tuning surface (TS), $f_{HE}^{ME}(\theta_H, \theta_E)$ (Figure 1B), was a 6×6 grid representing the mean FR for each combination of the six hand and six eye target angles (see STAR Methods).

For this example neuron, ME surfaces ($f_{HE}^{ME}(\theta_H, \theta_E)$) were able to be separated into one-dimensional TCs, ($f_H^{ME}(\theta_H)$ and $f_E^{ME}(\theta_E)$) (Figure 1C) (see STAR Methods). Conversely, its SE TCs ($f_H^{SE}(\theta_H)$ and $f_E^{SE}(\theta_E)$) were able to be additively composed into a two-dimensional TS ($f_{HE}^{SE}(\theta_H, \theta_E)$) (Figure 1F) (see STAR Methods). Together, these results provide a conceptual framework for how joint H-E representations can be disentangled and equivalently how separate hand and eye representations can be additively composed.

Single-neuron representations are additively separable

A TS is additively separable $F(\theta_H, \theta_E) = f(\theta_H) + f(\theta_E)$ if and only if it has no cross-partial derivatives $\partial^2 F(\theta_H, \theta_E)/\partial\theta_H\partial\theta_E = 0$ (see STAR Methods). In other words, TSs separate into independent components when the encoded variables do not interact. TS cross-derivatives were calculated with centered wrap-around finite-difference calculations (see STAR Methods). Every neuron in MC and SPL was subject to a separability test using the cross-partial derivative of its TS (Hz/rad^2) (see STAR Methods). The q values for all neurons in both areas, arising from the separability test, create two distributions (Figures 2A and 2H). Because neurons in MC do not commonly encode eye movements, they should be trivially separable $F(\theta_H, \theta_E) = f(\theta_H) + 0$. Consistent with that, all 251 (100%) neurons in MC were found to have no significant cross-derivative energy and thus were additively separable. In SPL, 127 (79%) neurons were found to have no significant cross-derivative energy, while 34 (21%) neurons were found to have TSs with cross-derivative energy greater than a random surface.

To better understand the subset of SPL neurons exhibiting significant interaction terms, we decomposed their TSs into additive and residual interaction components (see STAR Methods; Figures S1A–S1F). Although these neurons contained statistically significant interaction structure, the additive component remained substantially larger than the residual interaction component. Across the 34 SPL neurons with significant interaction terms, the average peak-to-peak amplitude of the additive component was 1.43 ± 0.15 Hz (SEM) compared to 0.73 ± 0.06 Hz for the residual interaction component, corresponding to an additive-to-residual amplitude ratio of 1.93. Likewise, on average, the residual interaction component accounted for only 26.7% of the total surface variance. Thus, the majority of firing-rate modulation remained attributable to the additive hand and eye representations. Interestingly, the residual interaction component was not random. Instead, it exhibited a structured relational code organized around the congruent and anti-congruent H-E movement axes (Figures S1G–S1M). On average, 55.9% of the residual representation peaks were concentrated along these relational axes compared to 33.3% expected from a uniform distribution. However, because this interaction structure remained substantially weaker than the dominant additive components, these neurons can still be reasonably approximated as additively separable, with the residual interaction terms acting primarily as a structured source of modeling error.

Treating all neurons as approximately separable, we quantified the relative encoding strength of each variable and their interactions using a Hessian matrix. Hessian matrices capture the local curvature of a function by calculating its second-order partial derivatives. In the context of neuronal representations of two behavioral variables, the elements of a 2×2 Hessian reflect how sharply a neuron's FR changes with respect to hand and eye movements, either independently (diagonal terms) or jointly (off-diagonal terms) (see STAR Methods). If a TS is additively separable, its Hessian should be diagonal over its whole domain, with no cross-partial derivatives. Across all neurons in MC, the average value of the Hessian's symmetric off-diagonal terms was 0.12 ± 0.01 Hz/rad^2 (SEM), while the diagonal terms were

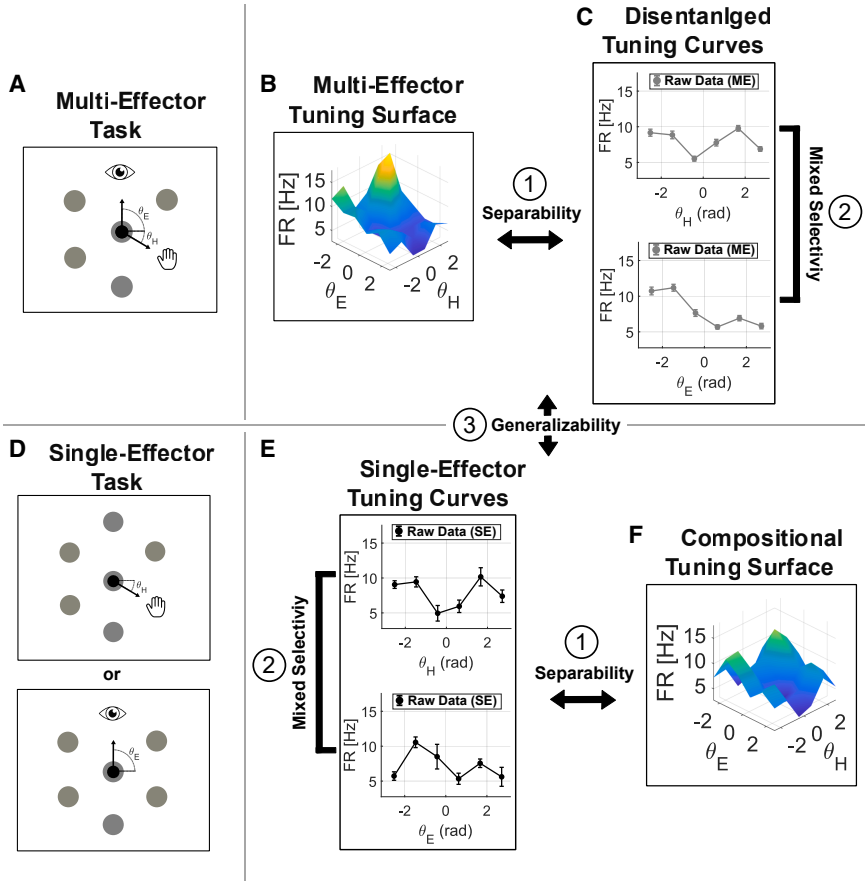


Figure 1. Single-session overview of task, representations, and properties

(A) Schematic of the ME center-out task: two simultaneous targets (hand and eye) are presented at angular locations θ_H and θ_E.

(B) Example SPL neuron's ME TS—FR as a function of hand and eye angles (θ_H and θ_E); surface color encodes FR (Hz) magnitude.

(C) TCs derived from separating the ME TS (projections along θ_H and θ_E). Points are means of the raw FR at each angle; error bars are the standard error of the mean (SEM).

(D) Schematic of the SE tasks: isolated hand or eye movements are performed on separate trials.

(E) TCs from SE trials (hand, eye), plotted as mean ± SEM of FR.

(F) Additive SE surface formed by composing the two SE TCs (hand + eye + constant) on the (θ_H and θ_E) grid.

(B), (C), (E), and (F) are representations from an example neuron from the SPL of PPC.

0.82 ± 0.06 Hz/rad^2 and 0.26 ± 0.02 Hz/rad^2 for the hand and eye second derivatives, respectively (Figure 2B). Similarly, for all neurons in SPL, the average value of the off-diagonal terms was 0. 10 ± 0.01 Hz/rad^2 and the diagonal terms were 0.49 ± 0.04 Hz/rad^2 and 0.33 ± 0.02 Hz/rad^2 for the second derivative of the hand and eye, respectively (Figure 2I). The interaction curvature strength was 20% of the hand curvature strength and 30% of the eye curvature strength, as measured by root mean square (RMS) deviation. So, across the population, the average interaction curvature was much weaker than primary effector curvature.

Separable TSs can be expressed as a simple sum of independent TCs ($f_{HE}^{ME}(\theta_H,\theta_E) = g_H^{ME}(\theta_H) + h_E^{ME}(\theta_E)$). In the ME context, independent TCs for the hand ($g_H^{ME}(\theta_H)$) and eye ($h_E^{ME}(\theta_E)$) can be obtained by projecting the ME TS onto one behavioral variable (averaging/marginalizing over the other variable) and centering (see STAR Methods). The ME TS ($f_{HE}^{ME}(\theta_H, \theta_E)$) (Figures 2C and 2J) and projected TCs ($g_H^{ME}(\theta_H)$ and $h_E^{ME}(\theta_E)$) (Figures 2D and 2K) are visualized for an example neuron from each brain area. For both example neurons, the reconstructed additive surfaces $\hat{f}_{HE}^{ME}(\theta_H,\theta_E) = g(\theta_H) + h(\theta_E)$ (Figures 2E and 2L) were good approximations of the pre-projection empirical ME TS (MC: R^2 = .9; PPC: R^2 = .69).

To quantify reconstruction quality across all neurons, we compared $f_{HE}^{ME}(\theta_H,\theta_E)$ and $\hat{f}_{HE}^{ME}(\theta_H,\theta_E)$ over the common 6 × 6 grid using a weighted coefficient of determination (see STAR Methods). The mean of the per-neuron R^2 distribution was .64 in MC and .57 in SPL; therefore, the average additively reconstructed surfaces were moderately linearly related to their raw empirical counterparts (Figures 2F and 2M). Across the distribution of all neurons, the average Pearson correlation coefficients (ρ) between the raw and reconstructed TSs was .79 in MC and .74 in SPL, indicating a consistently positive and strong linear

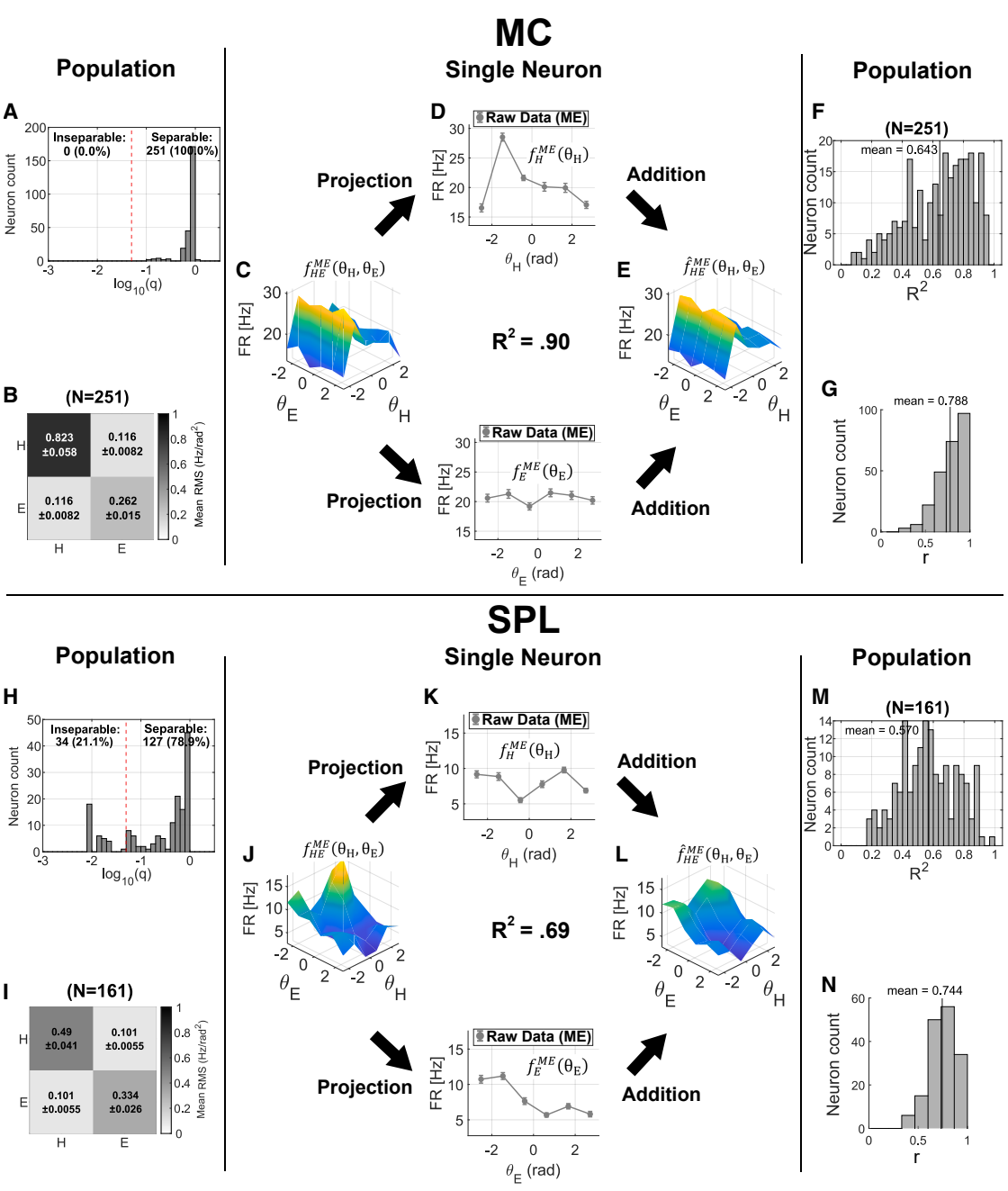


Figure 2. Separability of individual neurons during ME task

(A–G) Summarize the separability of neurons in the MC whereas (H–N) summarize the separability of neurons in the SPL. (A) Histogram of separability permutation test log(q) values for all neurons in MC. Significant q values (left of the red significance threshold (α = 0.05)), imply the cross-partial derivative RMS of the raw surface is significantly greater than a random surface. (B) Heatmap showing the average values of the Hessians calculated for every neuron's TS. Values are overlaid as mean ± SEM across neurons. (C) Example neuron's TS $f_{HE}^{ME}(\theta_H, \theta_E)$ from the ME task. Axes: hand direction θ_H (x), eye direction θ_E (y), FR (z; color also encodes FR). Directions are sampled on a 6 × 6 grid. (D) Projections of the TS in image (C): hand tuning $f_H^{ME}(\theta_H)$ (top) and eye tuning $f_E^{ME}(\theta_E)$ (bottom), obtained by averaging across the other effector. Points show means across trials; error bars show SEM. (E) Additive reconstruction $\hat{f}_{HE}^{ME}(\theta_H, \theta_E) = f_H^{ME}(\theta_H) - \overline{f_H^{ME}} + f_E^{ME}(\theta_E) - \overline{f_E^{ME}} + c$, where $\overline{f_H^{ME}}$, $\overline{f_E^{ME}}$ are the means of the TCs and c is a neuron-specific baseline estimated from the grand mean of the ME data. Axes and scale match image (C). (F) Distribution (histogram) of per-neuron reconstruction quality, reported as the coefficient of determination (R^2) between the raw surface (in image C) and the additive reconstruction (in image E). The total number of neurons contributing to the histogram is indicated on the image (e.g., N = 251).

(G) Distribution (histogram) of per-neuron Pearson correlation coefficient between the raw surface (image C) and the additive reconstructed surface (image E) across all neurons.

(H–N) These images depict the same visuals as (A–G) but for the SPL.

association between the surfaces of all neurons (Figures 2G and 2N).

Finally, while the data suggest that neural representations are separable on the single neuron level, it is common to investigate if separability extends to population codes. Conveniently, it is possible to analytically prove that if all neurons are additively separable, then any linear projection of the population activity will also be separable (see STAR Methods). We tested this implication for each session and identified a demixed additive basis where the projected population activity was additively separable, as evidenced by a parallelogram structure in the population latent space (Figure S2). The variety of measures reported here provides convergent empirical evidence that neurons in both brain regions can be reasonably treated as additively separable.

Neurons in SPL are mixed selective

After establishing separability of single-neuron representations, it is justified to treat projections of TSs as single-variable TCs. Projected ME TCs and empirical SE TCs were used to calculate selectivity of all recorded neurons. Commonly, selectivity is determined by an ANOVA. However, we found the distribution of data for each trial condition to be heteroskedastic with non-Gaussian FR residuals, thereby violating the assumptions of ANOVAs (Figure S3). This motivated the use of a nonparametric approach to assess tuning significance. The nonparametric approach we used was a permutation test of TC amplitude (A_X^C; Figures 3A and 3F), with significance determined from Benjamini-Hochberg-adjusted q values ($q_{X,med}^C$) computed across bootstrap resamples (see STAR Methods). Neurons were assigned to four classes by significance testing: "hand" or "eye" if only one effector's TC amplitude was significantly above baseline; "both" if both were; and "none" if none were. This analysis revealed a marked difference in effector selectivity between the two cortical areas. In MC (Figure 3B), the population was dominated by hand-selective neurons ($\approx$85%), with very few eye-selective (<1%) or mixed-selective ($\sim$1%) units, and a minority of non-selective neurons ($\approx$14%). In contrast, SPL (Figure 3G) exhibited a large population of mixed-selective neurons ($\approx$50%), alongside hand-selective ($\approx$39%), eye-selective ($\approx$4%), and non-selective ($\approx$7%) neurons.

In addition to selectivity, we also specifically investigated single-neuron activity during congruent H-E movements (both effectors directed to the same target) and incongruent H-E movements (effectors directed to different targets). Comparisons of mean FRs revealed that neurons generally exhibited similar levels of activity across congruent and incongruent conditions. Thus, we did not observe any evidence for preferential encoding of any specific combination of movements (Figures S4D and S4L).

Neuronal representations are generalizable across experimental contexts

To assess generalizability of the representations across ME and SE contexts, projected ME TCs (f_H^{ME} & f_E^{ME}) were compared to empirical SE TCs (f_H^{SE} & f_E^{SE}) in both MC (Figure 3C) and SPL (Figure 3H). Two metrics were used for comparison, TC peak-to-peak amplitude A_X^C (Figures 3D and 3I) and preferred direction (PD) PD_X^C (Figures 3E and 3J) (see STAR Methods).

In the MC, hand-selective neurons (making up $\approx$ 85% of MC neurons) demonstrated hand TCs with highly correlated amplitudes and PDs between the ME and SE contexts (r = .75 and r = .82 respectively) (Figures 3D and 3E). In the SPL, mixed-selective neurons (making up $\approx$ 50% of SPL neurons) demonstrated preservation of both hand and eye representations across contexts. Hand TCs showed high correlation of amplitudes and PDs across contexts (r = .60 and r = .58 respectively). Eye TCs showed moderate correlation of amplitudes (r = .45) but weaker correlation of PD (r = .15) across contexts. While present, eye representations in SPL were generally weaker and noisier than hand representations.

Projected ME TCs have a baseline FR equal to the grand mean of the ME TS, which is affected by both hand and eye movements. SE TCs, which involve movement of only one variable, have baseline FRs that differ from those of coordinated movements. This discrepancy is most apparent for eye TCs in MC (Figure 3C). Because eye movements are not encoded in MC, the SE eye TC baseline is low, whereas the projected ME eye TC baseline is elevated due to the influence of concurrent hand movements. When composing SE TCs into surfaces, we accounted for this by calculating the predicted baseline FR for the TS as a linear combination of the SE baselines (see STAR Methods).

Despite being well correlated, ME TCs showed systematically higher Z-scored peak-to-peak amplitudes than their SE counterparts (Figures 3D and 3I). This is caused by greater variation in the SE TC amplitudes, in part due to a fewer number of SE trials. Across 251 neurons in the MC, hand TC amplitudes had an average coefficient of variation (CV) of .15 for ME data but .24 for SE data. Across 161 neurons in the SPL, hand TC amplitudes had an average CV of .20 for ME data and .26 for SE data. This systematic difference in CV resulted in a greater-than-one ratio between ME and SE Z-scored amplitudes across neurons in both brain areas (Figures 3D and 3I).

Together, these results show that SPL contains many mixed-selective neurons whose hand and eye tunings are both generalizable from the SE to ME context. The SPL population is therefore separable, mixed-selective, and generalizable. Subsequently, these properties can be leveraged to build compositional, SE-derived generative models capable of decoding ME movements.

Composed single-effector models decode multi-effector behaviors

After establishing that a subset of PPC neurons was additively separable, mixed-selective, and generalizable, it was possible to create compositional surfaces from SE data that are comparable to the raw ME surfaces. If the two surfaces are effectively the same, from the perspective of likelihood evaluation, their decoding performance should also coincide.

Using the ME data (Figures 4A and 4B), we estimated each neuron's TS $f_{HE}^{ME}(\theta_H, \theta_E)$ from 216 training trials (36 H-E combinations $\times$ 6 repeats). For the SE data (Figures 4C and

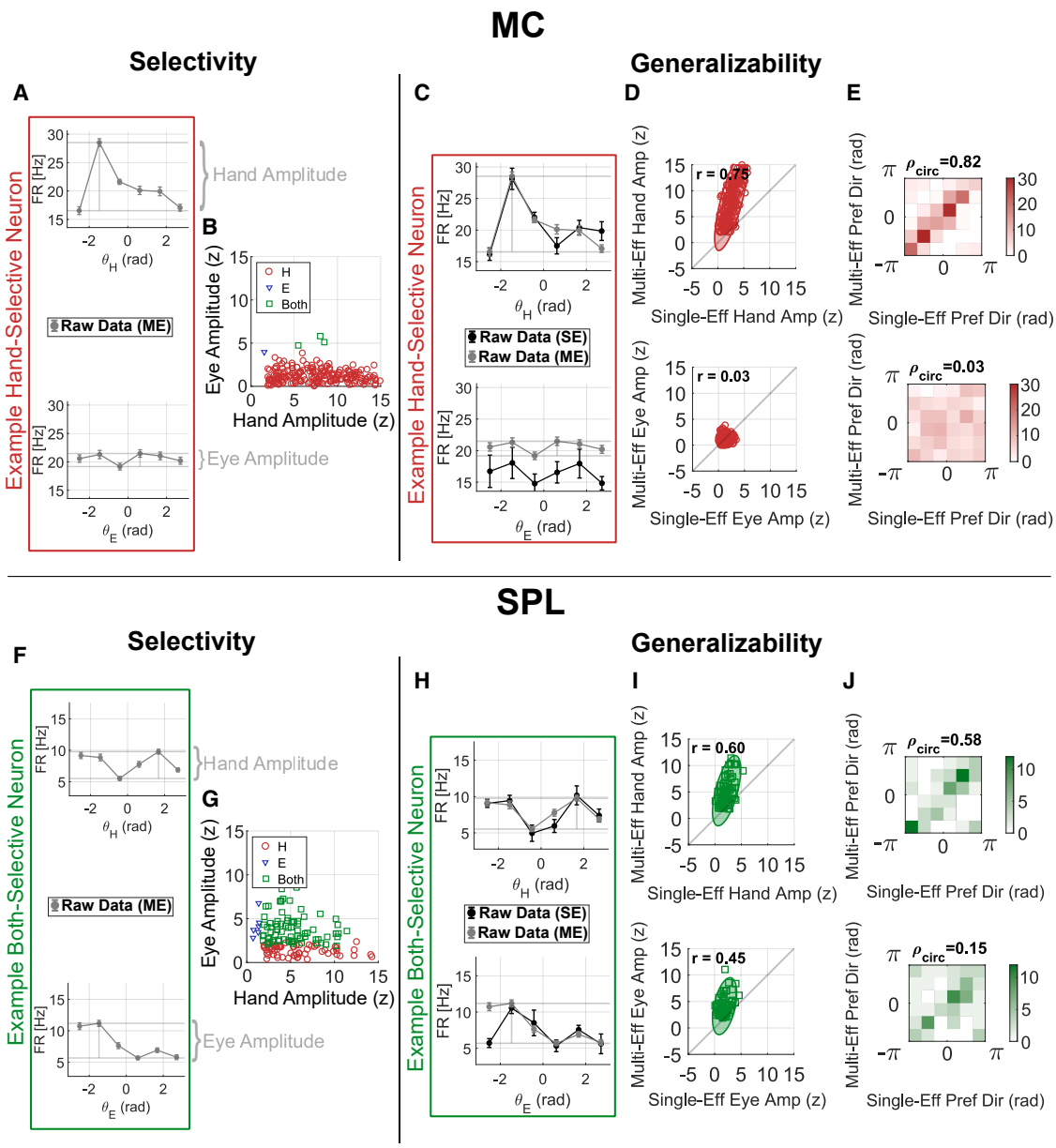


Figure 3. Selectivity and generalizability of single neurons in MC and SPL

(A–E) Summarize the selectivity and generalizability of neurons in the MC. (A) Example hand and eye TCs; light gray horizontal lines mark TCs' peak and trough, and a vertical line marks the TCs' PD. (B) Population scatter of *Z*-scored TC amplitudes (hand vs. eye) for all neurons; points are colored and shaped by the selectivity permutation test outcome (red circle, H; blue triangle, E; green square, both). (C) Overlaid ME (gray) and SE (black) TCs for an example hand-selective neuron (red outline). (D) Scatter of *Z*-scored amplitudes in SE (*x* axis) versus ME (*y* axis) for hand-selective neurons, with Pearson r reported. (E) Confusion matrix comparing SE and ME PDs for the same neurons. (F) Amplitude definition on example TCs.

(G and H) (G) Population amplitude scatter with the same color code; (H) overlaid ME (gray) and SE (black) TCs for an example both-selective neuron (green outline).

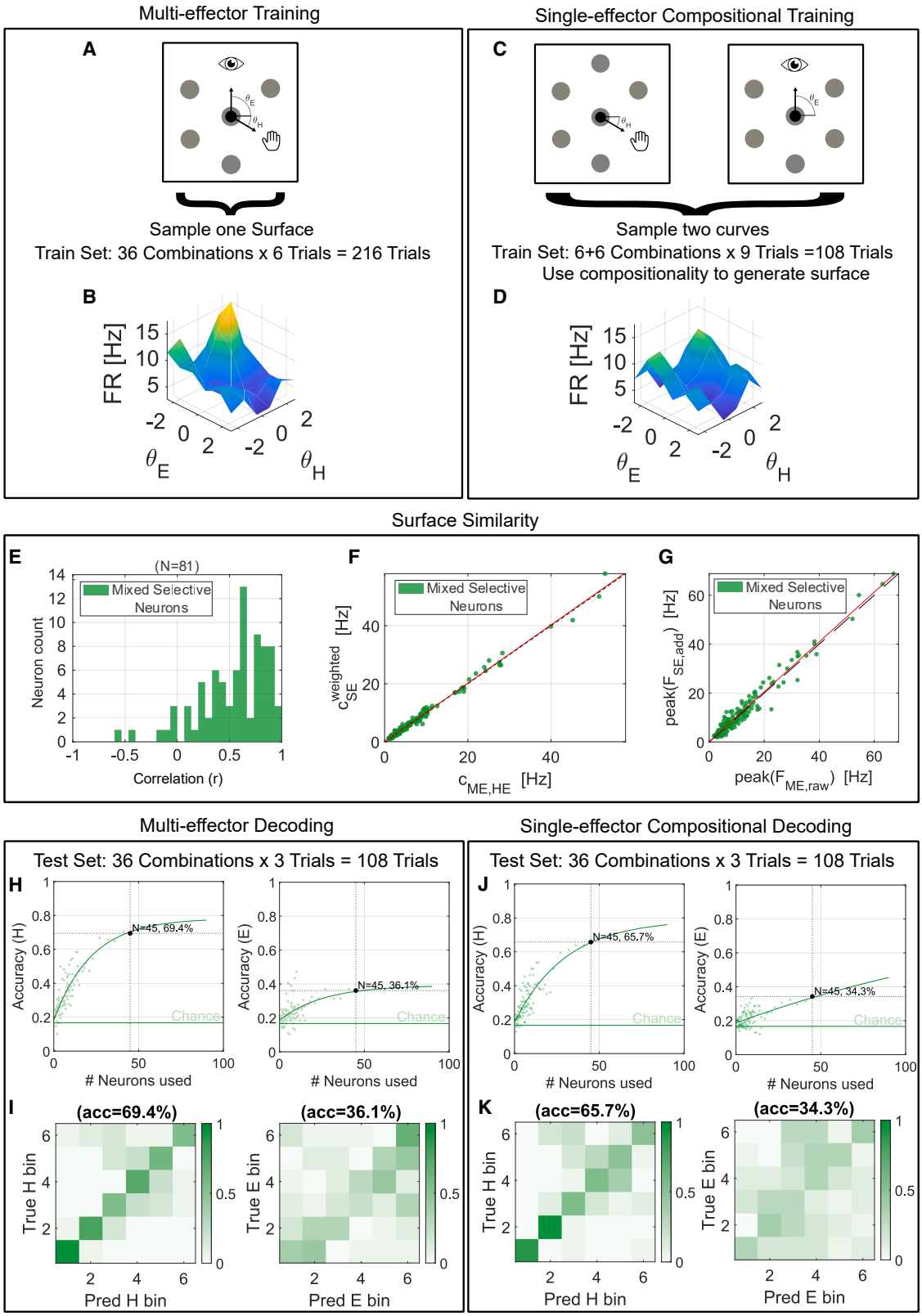
(I) SE-ME amplitude scatter for both-selective neurons, Pearson r reported.

(J) Confusion matrix comparing SE and ME PDs for the same both-selective neurons.

Images (F–J) share a parallel structure to (A–E) but for neurons in SPL.

Points in panels (A, C, F, H) show mean firing rates; error bars indicate the standard error of the mean (SEM).

4D), we estimated the compositional TS $\widehat{f}^{SE}_{HE}(\theta_H, \theta_E)$ by summing two SE TCs per neuron (hand $f^{SE}_{H}(\theta_H)$ and eye $f^{SE}_{E}(\theta_E)$) estimated from 108 SE training trials (6 directions × 9 repeats × 2 effectors). Three similarity metrics, Pearson correlation, grand mean FR, and peak FR, all showed that the SE-based compositional surfaces closely matched the raw ME TSs (Figures 4E–4G).



(legend on next page)

For all surfaces, we used circular kernel regression to obtain a smooth, continuous estimate of the mean FR at any behavioral state (see STAR Methods). Using this kernel, we defined a likelihood $p(r_{ref}|\theta)$ for each surface given an observed FR (r_{ref}). Assuming conditional independence of neurons we created a population likelihood by summing the log-likelihoods across neurons. We used the agreement of the independent neuron likelihoods in the population, as well as assuming a uniform prior over Θ, to perform Maximum a Posteriori (MAP) estimation of effector state (see STAR Methods). This enabled the creation of two MAP-based decoders, one for the SE-based compositional surfaces and another for the raw ME surfaces. MAP decoding accuracies are presented as the fraction of test trials with correctly inferred H-E state (between 6 discrete bins accuracy from pure chance is 16.67%). The accuracy of both MAP decoders was evaluated on the same held-out ME test set of 108 trials per session (36 combinations × 3 repeats).

Using an empirical maximum of 45 mixed-selective neurons, ME decoding accuracies for hand and eye movements were 69% and 36%, respectively, while SE decoding accuracies were 66% and 34%. Inverted dropping curves (Figures 4H–4K) further demonstrated near-identical accuracy scaling for ME- and SE-trained models, with saturating fits that extrapolated to similar ceilings (see STAR Methods). However, only 14.6 SPL neurons, on average, were recorded simultaneously per session. Therefore, when using the full recorded population from each session, mean hand and eye decoding accuracies were 42.2% and 27.7%, respectively, for the ME-trained decoder, compared with 37.8% and 24.5% for the SE-additive decoder.

We also examined decoding error across various H-E target combinations (Figure S4). Although very modest variation in decoding error was observed across target combinations, there was no evidence of systematic differences in decoding performance across movement conditions in either brain area (Figures S4E, S4H, S4M, and S4P). In particular, we evaluated decoder performance separately for congruent and incongruent H-E target combinations. In SPL, average ME-model-based decoding error was 58° for congruent trials and 62° for incongruent trials, while average SE-model-based decoding error was 67° and 69°, respectively (chance decoding error = 90°; Figures S4M–S4P). These results suggest that decoding accuracy was relatively uniform across the sampled movement space.

Because MC exhibited negligible eye-related modulation and therefore did not support a meaningful H-E compositional model, the compositional decoding analyses (Figure 4) were restricted to SPL. However, to explore whether MC provides complementary information during coordinated movements, we also trained ME decoders using the combined MC and SPL population. Pooling the two regions modestly increased hand-decoding accuracy relative to SPL alone (52.8% versus 42.2%) but left eye-decoding accuracy essentially unchanged (28.3% versus 27.7%), consistent with MC contributing primarily hand-related information (Figure S5).

Despite the ME model being trained with twice as many trials as the SE-based compositional model (216 trials vs. 108 trials), the compositional model achieved roughly the same decoding accuracy when evaluated on the same test set. The SE-based decoding succeeded precisely because the SE-composed surface $\widehat{f}^{SE}_{HE,n}(\theta_H, \theta_E)$ was an accurate surrogate for the ME surface $f^{ME}_{HE,n}(\theta_H, \theta_E)$. Therefore, the decoding results and representational similarity metrics are decisive evidence of the compositional coding of single neurons in PPC during the execution of an H-E coordinated center-out task.

DISCUSSION

The central result of this study is that, in the SPL of PPC, hand- and eye-movement codes are independent components of the neural representations arising from H-E coordinated movements during conventional center-out tasks. This is significant because it implies that, in SPL, eye-movement activity can be disentangled or marginalized over during the decoding of certain coordinated behaviors. We also demonstrate that separable codes can be used compositionally to decode coordinated movements from models trained on isolated movements. This work also develops a more general methodology for identifying compositionality with just three necessary and sufficient representational properties.

The first property, additive separability, ensures that ME TSs are well approximated by the sum of their one-dimensional

Figure 4. Compositional SE models decode behaviors about as well as ME models in SPL

(A) Schematic of the ME center-out task in which hand and eye targets at angles θ_H and θ_E are presented simultaneously. Training uses 216 trials per session (36 combinations × 6 repeats).

(B) Example TS $\boldsymbol{f(\theta_H,\theta_E)}$ derived from ME raw data (surface height and color encode FR).

(C) Schematic of the SE tasks in which hand and eye movements are executed on separate trials in the same six directions; training uses 108 trials per session (hand: 6 × 9; eye: 6 × 9).

(D) Additive compositional surface constructed from SE curves.

(E) Histogram of Pearson correlation coefficients between ME and SE TSs for 81 mixed selective neurons in SPL.

(F) Scatterplot of baseline FR for the raw ME surface versus additive SE surfaces of 81 both selective neurons.

(G) Scatterplot of peak FR for the raw ME surface versus additive SE surface for same 81 neurons.

(H) Inverse dropping curve: hand (left) and eye (right) decoding accuracy as a function of the number of neurons used in inference; light green points are per-session accuracies and dark green curves are saturating fits extrapolated beyond the observed range.

(I) Decoding confusion matrices for hand (left) and eye (right) from the session with most neurons; rows are true bins, columns are predicted bins, values are row-normalized, and mean diagonal accuracy is shown above each matrix.

(J) Inverse dropping curve but for the accuracy of prediction with the compositional model (format as in H; same ME test set).

(K) Decoding confusion matrices for the compositional decoder (format as in I).

All images use only SPL data. (H–K) enable a direct, like-for-like comparison between ME-trained and SE-trained decoding on an ME test set of 108 trials per session (36 hand-eye combinations × 3 repeats).

projections (Figure 2). In SPL, 79% of neurons had neural representations that were additively separable into independent hand- and eye-movement TCs with no significant variable interactions. While 21% of neurons in SPL had representations with structured variable interactions, the interactions were weaker than the still-present separable hand and eye components. To identify additive separability in neural representations, we use cross-derivative energy as diagnostic tool (Figures 2A, 2B, 2H, and 2I). Zero cross-derivative energy alone is necessary and sufficient for additive separability (see STAR Methods). Beyond H-E coordination, the cross-derivative framework also generalizes naturally: in n variables, additive separability corresponds to a diagonal Hessian over the full domain and the vanishing of all mixed finite differences. We also posit that this representational feature could be embedded into learning objectives by penalizing cross-derivative energy, thereby biasing models toward additive, compositional solutions.

The second property, mixed selectivity,[48] establishes that the separable projections of TSs are significantly correlated with more than one behavioral variable. Here, the contrast between SPL and MC was stark. MC neurons were overwhelmingly hand-tuned, with negligible encoding of eye movements (Figures 3A and 3B). In contrast, approximately half of neurons in SPL were significantly tuned to both the hand and eye (Figures 3F and 3G). These findings are consistent with known differences in functional specialization between MC and SPL. The MC has many subregions, each of which encodes the motor commands of specific body parts with few confounding signals. Meanwhile, the SPL encodes movement commands across many parts of the body, including the hand and eye, and potentially movement in a common distributed space.[26,49] This perspective is supported by similar decoding accuracy of congruent and incongruent H-E movements (Figure S4). These observations are consistent with the broader finding that SPL neurons do not preferentially encode specific H-E target combinations, but instead represent hand and eye movement directions through separable mixed-selective tuning.

The third property, generalizability, guarantees that independent neural codes are consistent across single- and ME behavioral contexts. In SPL, the amplitude and PD of hand-movement representations were moderately to strongly correlated between SE and ME contexts. Meanwhile, for eye-movement representations, amplitude and PD were only moderately correlated between contexts, in part driven by weaker overall encoding strength (Figures 3I and 3J). These results indicate that SPL provides stable, reusable representations of both hand and eye, with an evident asymmetry in strength.

When these conditions hold simultaneously, models assembled solely from SE-derived modular TCs can be used to accurately decode ME behaviors. A compositional decoder trained solely on SE data achieved comparable decoding performance on held-out ME trials as a decoder trained directly on ME TSs, despite the latter having twice as many training samples (Figures 4I–4K). This equivalence demonstrates the advantages afforded by compositionality. The ability to build accurate ME decoders from reusable SE modules suggests that future BMIs could exploit compositional codes to reduce training demands and improve versatility of BMIs.[40–42] Moreover, this modular encoding strategy also facilitates the subtraction of unwanted separable neural codes, thereby improving decoding performance in the presence of confounding behavioral variables. If a similar compositional structure extends to additional effectors encoded in PPC, this region may represent a promising target for future BMI implantation.

Another contribution of this work is the demonstration of simple, nonparametric likelihood-based decoders. When making scientific deductions, decoding performance is commonly used as a proxy for representational structure in BMI studies.[34,46] However, likelihood-based decoders directly link representation geometry to decoding performance. This link shifts the construction of compositional decoders to the representational level, where additive neural components can be combined intuitively and then mapped to decoding.

While these findings largely concern single-neuron representations, we also proved that single-neuron additive separability guarantees additive separability of population codes under linear projections (see STAR Methods and Figure S2). Mixed selectivity and generalizability trivially extend to population codes as well. This unifies single-neuron- and population-level conclusions. However, it also emphasizes that, at both the single neuron and population level, neurons in SPL can be treated as additively compositional.

In summary, these results show that neurons in SPL of PPC employ separable, mixed-selective, and generalizable encodings of H-E coordinated movements during common BMI tasks. Together, these properties establish a framework for identifying compositionality that can be applied beyond this study. Compositionality is a particularly useful principle, as it directly links modular neural representations to modular decoding architectures and enables neural decoders to generalize beyond their training conditions. This study provides a foundation for future work examining when modular neural codes can be extracted and leveraged to build more flexible ME BMIs.

Limitations of the study

First, all data were obtained from a single participant, making this work a case study. While the findings provide a proof of principle that SPL neurons exhibit compositional coding of H-E movements, broader generalization will require replication in additional participants and in neighboring brain regions to establish whether the observed properties are consistent across individuals and cortical areas.

Second, the experimental design imposes constraints on how hand and eye representations can be dissociated. Because participants must use their eyes to perceive target cues, it is difficult to elicit hand movements independently of eye movements. Consequently, small eye movements occasionally occur during trials that are misaligned with the goal/eye target. This coupling creates a potential confound, as eye activity is inextricably linked to the command structure of hand movements in this task. We did not observe any consistent behavioral confounds due to this task structure, but it likely contributed to the noise floor of the experimental results. One possible solution is to study compositionality in naturalistic behaviors without explicit trial commands, where neural and behavioral activity can be analyzed post hoc.

The task design discretized both hand and eye movements into six directions, and all analyses were performed on the resulting 6 × 6 tuning grids. This coarse discretization may obscure finer-grained nonlinearities or interactions that only emerge in continuous movement spaces. Likewise, while the cross-derivative energy test is mathematically rigorous, finite differences on a sparse grid may lack sensitivity to local deviations from additivity. Thus, our conclusion of negligible interaction energy should be interpreted in light of the resolution limits imposed by the task and sampling.

Another limitation concerns the asymmetry of representations in SPL. While hand signals were robust, eye signals were consistently weaker and noisier. This asymmetry raises the possibility that neuronal representations in the SPL only appear additive compositionality due to the weakness of the eye representation. If the eye is weakly represented, then it is possible that variable interactions with the eye are weak as well. Extending the analysis to effectors with more balanced encoding strength, such as bimanual limb movements, may clarify whether compositionality is a universal property of SPL or a result of asymmetric encoding.

Finally, the decoding analyses rested on assumptions of conditional independence across neurons and time invariance of representations during recording sessions. Both assumptions are common in BMI modeling but are known simplifications of neural population dynamics. Dependencies across neurons or time-varying representations could alter the apparent degree of compositionality or its utility for decoding. Future work using larger-scale, simultaneous recordings and models that explicitly account for cross-neuronal correlations may provide a more complete picture.

Together, these limitations highlight the need for additional work to validate compositionality as a general coding principle. While the present study establishes a strong initial case in SPL, broader evidence across participants, brain areas, behavioral paradigms, and analytical frameworks will be essential to confirm its scope and robustness.

RESOURCE AVAILABILITY

Lead contact

Requests for further information and resources should be directed to and will be fulfilled by the lead contact, Nikos A. Mynhier (nmynhier@caltech.edu).

Materials availability

- This study did not generate new unique reagents.

Data and code availability

- The processed data supporting the findings of this study are publicly available through CaltechDATA: https://doi.org/10.22002/p50pc-49s61. The DOI is also listed in the key resources table.
- The analysis code used to generate the results and source plots reported in this study is publicly available through Zenodo: https://doi.org/10.5281/zenodo.22969624. The DOI is also listed in the key resources table.
- Any additional information required to reanalyze the data reported in this paper is available from the lead contact upon request.

ACKNOWLEDGMENTS

We thank participant RD for engaging in our clinical trial. This work was funded by the National Eye Institute Award UG1EY032039A, the T&C Chen Brain-Machine Interface Center, and the James G. Boswell Foundation. The human sitting illustration used in the graphical abstract was adapted from Servier Medical Art (https://smart.servier.com), licensed under CC BY 4.0. We thank Viktor Scherbatyuk for IT support. We thank Sunho Lee and Vasiliki Bougou for reviewing the manuscript.

AUTHOR CONTRIBUTIONS

Conceptualization, N.A.M., R.A.A., J.G. K.P.M., and R.M.M.; methodology, N.A.M., K.P.M., and J.G.; investigation, N.A.M.; writing – original draft, N.A.M.; writing – review and editing, R.A.A., J.G., R.M.M., and K.P.M.; funding acquisition, R.A.A., K.P., J.G., and N.A.M.; resources, R.A.A., K.P., and R.M.M.; clinical trial management, K.P., R.A.A., and J.G.; supervision, R.A.A., R.M.M., and J.G.; surgical and medical intervention, A.B.

DECLARATION OF INTERESTS

Richard M. Murray serves on the board of Convergent.

DECLARATION OF GENERATIVE AI AND AI-ASSISTED TECHNOLOGIES IN THE MANUSCRIPT PREPARATION PROCESS

During the preparation of this work, the authors used ChatGPT to proofread including the revision of grammar, syntax, and structure of written text. ChatGPT was also used to verify and condense code used for data analysis. After using this tool or service, the authors reviewed and edited the content as needed and take full responsibility for the content of the publication.

STAR★METHODS

Detailed methods are provided in the online version of this paper and include the following:

- KEY RESOURCES TABLE
- EXPERIMENTAL MODEL AND STUDY PARTICIPANT DETAILS
- METHOD DETAILS
  - Experiment/multi-effector task
  - Neural signal recording and processing
  - Empirical tuning curves and surfaces
  - Additive separability is equivalent to zero cross-partial derivatives
  - Separability calculations
  - Two pass smoothing
  - Cross Derivative Finite Difference
  - Root-Mean-Squared Calculation
  - Projections and Additive Surfaces
  - Residual surfaces
  - Representation Similarity Metrics
  - Weighted SE baseline
  - Proof of population separability
  - Circular Kernel Mean and Variance
  - Bayesian Inference
  - Inverted dropping curve
- QUANTIFICATION AND STATISTICAL ANALYSIS
  - Weighted coefficient of determination
  - Separability Permutation Test
  - Selectivity permutation tests and bootstrapping
- ADDITIONAL RESOURCES

SUPPLEMENTAL INFORMATION

Supplemental information can be found online at https://doi.org/10.1016/j.celrep.2026.118204.

Received: April 13, 2026
Revised: August 6, 2026
Accepted: October 7, 2026

REFERENCES

1. Mishkin, M., Ungerleider, L.G., and Macko, K.A. (1983). Object vision and spatial vision: two cortical pathways. Trends Neurosci. *6*, 414–417. https://doi.org/10.1016/0166-2236(83)90190-X.
2. Medendorp, W.P., Goltz, H.C., Vilis, T., and Crawford, J.D. (2003). Gaze-Centered Updating of Visual Space in Human Parietal Cortex. J. Neurosci. *23*, 6209–6214. https://doi.org/10.1523/JNEUROSCI.23-15-06209.2003.
3. Connolly, J.D., Goodale, M.A., Desouza, J.F.X., Menon, R.S., and Vilis, T.; The Medical Research Council Group for Action and Perception (2000). A comparison of frontoparietal fMRI activation during anti-saccades and anti-pointing. J. Neurophysiol. *84*, 1645–1655. https://doi.org/10.1152/jn.2000.84.3.1645.
4. Andersen, R.A., Essick, G.K., and Siegel, R.M. (1985). Encoding of spatial location by posterior parietal neurons. Science *230*, 456–458. https://doi.org/10.1126/science.4048942.
5. Vesia, M., and Crawford, J.D. (2012). Specialization of reach function in human posterior parietal cortex. Exp. Brain Res. *221*, 1–18. https://doi.org/10.1007/s00221-012-3158-9.
6. Batista, A.P., Buneo, C.A., Snyder, L.H., and Andersen, R.A. (1999). Reach Plans in Eye-Centered Coordinates. Science *285*, 257–260. https://doi.org/10.1126/science.285.5425.257.
7. Buneo, C.A., Jarvis, M.R., Batista, A.P., and Andersen, R.A. (2002). Direct Visuomotor Transformations for Reaching, *416*, p. 5.
8. Batista, A. (2002). Inner space: Reference frames. Curr. Biol. *12*, R380–R383. https://doi.org/10.1016/S0960-9822(02)00878-3.
9. Snyder, L.H., Batista, A.P., and Andersen, R.A. (1997). Coding of intention in the posterior parietal cortex. Nature *386*, 167–170. https://doi.org/10.1038/386167a0.
10. Snyder, L.H., Grieve, K.L., Brotchie, P., and Andersen, R.A. (1998). Separate body- and world-referenced representations of visual space in parietal cortex. Nature *394*, 887–891. https://doi.org/10.1038/29777.
11. Quiroga, R.Q., Snyder, L.H., Batista, A.P., Cui, H., and Andersen, R.A. (2006). Movement Intention Is Better Predicted than Attention in the Posterior Parietal Cortex. J. Neurosci. *26*, 3615–3620. https://doi.org/10.1523/JNEUROSCI.3468-05.2006.
12. Snyder, L.H., Calton, J.L., Dickinson, A.R., and Lawrence, B.M. (2002). Eye-Hand Coordination: Saccades Are Faster When Accompanied by a Coordinated Arm Movement. J. Neurophysiol. *87*, 2279–2286. https://doi.org/10.1152/jn.00854.2001.
13. Snyder, L.H., Batista, A.P., and Andersen, R.A. (2000). Saccade-Related Activity in the Parietal Reach Region. J. Neurophysiol. *83*, 1099–1102. https://doi.org/10.1152/jn.2000.83.2.1099.
14. Chang, S.W.C., Dickinson, A.R., and Snyder, L.H. (2008). Limb-Specific Representation for Reaching in the Posterior Parietal Cortex. J. Neurosci. *28*, 6128–6140. https://doi.org/10.1523/JNEUROSCI.1442-08.2008.
15. Chang, S.W.C., Papadimitriou, C., and Snyder, L.H. (2009). Using a Compound Gain Field to Compute a Reach Plan. Neuron *64*, 744–755. https://doi.org/10.1016/j.neuron.2009.11.005.
16. Salinas, E., and Sejnowski, T.J. (2001). Gain Modulation in the Central Nervous System: Where Behavior, Neurophysiology, and Computation Meet. Neuroscientist *7*, 430–440. https://doi.org/10.1177/107385840100700512.
17. Brozović, M., Abbott, L.F., and Andersen, R.A. (2008). Mechanism of gain modulation at single neuron and network levels. J. Comput. Neurosci. *25*, 158–168. https://doi.org/10.1007/s10827-007-0070-6.
18. Bremner, L.R., and Andersen, R.A. (2014). Temporal Analysis of Reference Frames in Parietal Cortex Area 5d during Reach Planning. J. Neurosci. *34*, 5273–5284. https://doi.org/10.1523/JNEUROSCI.2068-13.2014.
19. Bremner, L.R., and Andersen, R.A. (2012). Coding of the Reach Vector in Parietal Area 5d. Neuron *75*, 342–351. https://doi.org/10.1016/j.neuron.2012.03.041.
20. Pesaran, B., Nelson, M.J., and Andersen, R.A. (2006). Dorsal Premotor Neurons Encode the Relative Position of the Hand, Eye, and Goal during Reach Planning. Neuron *51*, 125–134. https://doi.org/10.1016/j.neuron.2006.05.025.
21. Hwang, E.J., Hauschild, M., Wilke, M., and Andersen, R.A. (2014). Spatial and Temporal Eye-Hand Coordination Relies on the Parietal Reach Region. J. Neurosci. *34*, 12884–12892. https://doi.org/10.1523/JNEUROSCI.3719-13.2014.
22. Crawford, J.D., Medendorp, W.P., and Marotta, J.J. (2004). Spatial Transformations for Eye–Hand Coordination. J. Neurophysiol. *92*, 10–19. https://doi.org/10.1152/jn.00117.2004.
23. Sabes, P.N., Breznen, B., and Andersen, R.A. (2002). Parietal Representation of Object-Based Saccades. J. Neurophysiol. *88*, 1815–1829. https://doi.org/10.1152/jn.2002.88.4.1815.
24. Pouget, A., and Sejnowski, T.J. (1997). Spatial transformations in the parietal cortex using basis functions. J. Cognit. Neurosci. *9*, 222–237. https://doi.org/10.1162/jocn.1997.9.2.222.
25. Pouget, A., and Snyder, L.H. (2000). Computational approaches to sensorimotor transformations. Nat. Neurosci. *3*, 1192–1198. https://doi.org/10.1038/81469.
26. Andersen, R.A., and Buneo, C.A. (2002). Intentional maps in posterior parietal cortex. Annu. Rev. Neurosci. *25*, 189–220. https://doi.org/10.1146/annurev.neuro.25.112701.142922.
27. Cohen, Y.E., and Andersen, R.A. (2002). A common reference frame for movement plans in the posterior parietal cortex. Nat. Rev. Neurosci. *3*, 553–562. https://doi.org/10.1038/nrn873.
28. Bushnell, M.C., Goldberg, M.E., and Robinson, D.L. (1981). Behavioral enhancement of visual responses in monkey cerebral cortex. I. Modulation in posterior parietal cortex related to selective visual attention. J. Neurophysiol. *46*, 755–772. https://doi.org/10.1152/jn.1981.46.4.755.
29. Christopoulos, V.N., Bonaiuto, J., Kagan, I., and Andersen, R.A. (2015). Inactivation of Parietal Reach Region Affects Reaching But Not Saccade Choices in Internally Guided Decisions. J. Neurosci. *35*, 11719–11728. https://doi.org/10.1523/JNEUROSCI.1068-15.2015.
30. Culham, J.C., and Valyear, K.F. (2006). Human parietal cortex in action. Curr. Opin. Neurobiol. *16*, 205–212. https://doi.org/10.1016/j.conb.2006.03.005.
31. Andersen, R.A., Andersen, K.N., Hwang, E., and Hauschild, M. (2014). Optic ataxia: from Balint's syndrome to the parietal reach region. Neuron *81*, 967–983. https://doi.org/10.1016/j.neuron.2014.02.025.
32. Khan, A.Z., Pisella, L., Rossetti, Y., Vighetto, A., and Crawford, J.D. (2005). Impairment of Gaze-centered Updating of Reach Targets in Bilateral Parietal–Occipital Damaged Patients. Cerebr. Cortex *15*, 1547–1560. https://doi.org/10.1093/cercor/bhi033.
33. Mesulam, M.-M. (1999). Spatial attention and neglect: parietal, frontal and cingulate contributions to the mental representation and attentional targeting of salient extrapersonal events. Phil. Trans. Roy. Soc. Lond. B *354*, 1325–1346. https://doi.org/10.1098/rstb.1999.0482.
34. Aflalo, T., Kellis, S., Klaes, C., Lee, B., Shi, Y., Pejsa, K., Shanfield, K., Hayes-Jackson, S., Aisen, M., Heck, C., et al. (2015). Decoding motor imagery from the posterior parietal cortex of a tetraplegic human. Science *348*, 906–910. https://doi.org/10.1126/science.aaa5417.
35. Noneman, K.K., and Patrick Mayo, J. (2025). Decoding Continuous Tracking Eye Movements from Cortical Spiking Activity. Int. J. Neural Syst. *35*, 2450070. https://doi.org/10.1142/S0129065724500709.
36. Land, M.F. (2006). Eye movements and the control of actions in everyday life. Prog. Retin. Eye Res. *25*, 296–324. https://doi.org/10.1016/j.preteyeres.2006.01.002.
37. Donchin, O., Gribova, A., Steinberg, O., Bergman, H., and Vaadia, E. (1998). Primary motor cortex is involved in bimanual coordination. Nature *395*, 274–278. https://doi.org/10.1038/26220.

38. Ifft, P.J., Shokur, S., Li, Z., Lebedev, M.A., and Nicolelis, M.A.L. (2013). A Brain-Machine Interface Enables Bimanual Arm Movements in Monkeys. Sci. Transl. Med. *5*. https://doi.org/10.1126/scitranslmed.3006159.

39. Downey, J.E., Quick, K.M., Schwed, N., Weiss, J.M., Wittenberg, G.F., Boninger, M.L., and Collinger, J.L. (2020). The Motor Cortex Has Independent Representations for Ipsilateral and Contralateral Arm Movements But Correlated Representations for Grasping. Cerebr. Cortex *30*, 5400–5409. https://doi.org/10.1093/cercor/bhaa120.

40. Willett, F.R., Deo, D.R., Avansino, D.T., Rezaii, P., Hochberg, L.R., Henderson, J.M., and Shenoy, K.V. (2020). Hand Knob Area of Premotor Cortex Represents the Whole Body in a Compositional Way. Cell *181*, 396–409.e26. https://doi.org/10.1016/j.cell.2020.02.043.

41. Shah, N.P., Avansino, D., Kamdar, F., Nicolas, C., Kapitonava, A., Vargas-Irwin, C., Hochberg, L., Pandarinath, C., Shenoy, K., Willett, F.R., and Henderson, J. (2025). Pseudo-linear summation explains neural geometry of multi-finger movements in human premotor cortex. Nat. Commun. *16*, 5008. https://doi.org/10.1038/s41467-025-59039-z.

42. Deo, D.R., Willett, F.R., Avansino, D.T., Hochberg, L.R., Henderson, J.M., and Shenoy, K.V. (2024). Brain control of bimanual movement enabled by recurrent neural networks. Sci. Rep. *14*, 1598. https://doi.org/10.1038/s41598-024-51617-3.

43. Abeles, M., Diesmann, M., Flash, T., Geisel, T., Herrmann, M., and Teicher, M. (2013). Compositionality in neural control: an interdisciplinary study of scribbling movements in primates. Front. Comput. Neurosci. *7*. https://doi.org/10.3389/fncom.2013.00103.

44. Willsey, M.S., Shah, N.P., Avansino, D.T., Hahn, N.V., Jamiolkowski, R.M., Kamdar, F.B., Hochberg, L.R., Willett, F.R., and Henderson, J.M. (2025). A high-performance brain–computer interface for finger decoding and quadcopter game control in an individual with paralysis. Nat. Med. *31*, 96–104. https://doi.org/10.1038/s41591-024-03341-8.

45. Zou, X., Gamez, J., Menon, M., Ring, P., Boulay, C., Chitneni, L., Brennecke, J., Melby, S.R., Kureel, G., Pejsa, K., et al. (2025). Control of a commercially available vehicle by a tetraplegic human using a brain-computer interface. Preprint at arXiv. https://arxiv.org/abs/2508.11805v2.

46. Guan, C., Aflalo, T., Kadlec, K., Gámez De Leon, J., Rosario, E.R., Bari, A., Pouratian, N., and Andersen, R.A. (2023). Decoding and geometry of ten finger movements in human posterior parietal cortex and motor cortex. J. Neural. Eng. *20*, 036020. https://doi.org/10.1088/1741-2552/acd3b1.

47. Zhang, C.Y., Aflalo, T., Revechkis, B., Rosario, E.R., Ouellette, D., Pouratian, N., and Andersen, R.A. (2017). Partially Mixed Selectivity in Human Posterior Parietal Association Cortex. Neuron *95*, 697–708.e4. https://doi.org/10.1016/j.neuron.2017.06.040.

48. Tye, K.M., Miller, E.K., Taschbach, F.H., Benna, M.K., Rigotti, M., and Fusi, S. (2024). Mixed selectivity: Cellular computations for complexity. Neuron *112*, 2289–2303. https://doi.org/10.1016/j.neuron.2024.04.017.

49. Kadlec, K., Gamez, J., Aflalo, T., Guan, C., Rosario, E.R., Pejsa, K., Bari, A., Pouratian, N., and Andersen, R. (2025). Distinct patterns of whole-body coding in human motor cortex and posterior parietal cortex. Preprint at medRxiv. https://doi.org/10.1101/2025.08.01.25332521.

50. Nadaraya, E.A. (1964). On Estimating Regression. Theory Probab. Appl. *9*, 141–142. https://doi.org/10.1137/1109020.

51. Watson, G.S. (1964). Smooth Regression Analysis. Sankhyā: The Indian Journal of Statistics, Series A (1961-2002) *26*, 359–372.

52. Mardia, K.V., and Jupp, P.E. (2000). Directional Statistics (J. Wiley).

STAR★METHODS

KEY RESOURCES TABLE

REAGENT or RESOURCE	SOURCE	IDENTIFIER
Deposited data		
Processed Data (FR and behavioral data matrices)	this paper	CaltechDATA: https://doi.org/10.22002/p50pc-49s61
Archived code for data analysis and figure production	this paper	Zenodo: https://doi.org/10.5281/zenodo.22969624
Software and algorithms		
MATLAB (R2024b)	The MathWorks Inc	https://www.mathworks.com
MATLAB - Statistics and Machine Learning Toolbox	The MathWorks Inc	https://www.mathworks.com/products/statistics.html
MATLAB - Parallel Computing Toolbox	The MathWorks Inc	https://www.mathworks.com/products/parallel-computing.html

EXPERIMENTAL MODEL AND STUDY PARTICIPANT DETAILS

This study included one human participant in a single group assignment. The participant (RD) was a 40-year-old white Hispanic male with an incomplete C3/C4 injury resulting in chronic quadriplegia with retained limited voluntary movement of the shoulders and proximal arm. Consequently, instructed reaches were attempted and partially-to-fully executed, whereas gaze shifts were fully executed. The participant was implanted with 64-channel NeuroPort Utah electrode arrays. Implant locations were determined using anatomical priors and preoperative fMRI (Figure S6). The first array was implanted in the Superior Parietal Lobule (SPL) in the PPC. The second array was implanted in the Supramarginal Gyrus (SMG) of the PPC. SMG was found to not respond to hand and eye movements and was thus not used in this study. The third and fourth arrays (MCM and MCL) were implanted in medial and lateral regions of the motor cortex hand knob, respectively. Due to functional similarity, these arrays were pooled and analyzed as a single motor cortex (MC) population.

The human studies presented in this work are approved and overseen by the institutional review boards of the California Institute of Technology (IR23-0401), University of California Los Angeles (IRB-13–0576-AM-040), and Casa Colina Rehabilitation Center (IRB00002372). Informed consent was obtained from all enrolled subjects.

METHOD DETAILS

Experiment/multi-effector task

We developed a multi-effector center-out task (Figures 1A and 1D) to induce coordinated hand–eye movements (Video S1). The task consisted of a central fixation marker and six peripheral markers positioned at a fixed radial distance from the center. During multi-effector (ME) trials, two targets were presented at the six peripheral locations. The participant was instructed to simultaneously perform a reach (hand movement) toward one target and a gaze shift (eye movement) toward the other target displayed on the screen. This produced 36 (6×6) possible hand–eye target combinations, including trials in which both targets appeared at the same location.

During single-effector (SE) trials, only one target was presented at one of the six peripheral locations. Separate hand-only and eye-only movements generated an additional 12 trial types (6 hand targets +6 eye targets). Finally, a single rest trial was included as a control, in which both targets were presented at the central marker and no movement was instructed. In total, the task contained 49 trial types, each repeated three times within a block, resulting in 147 trials per block. On each of the 11 recording sessions, the block was performed two or three times.

During a block, trials were pseudo-randomly interleaved such that all 147 trials were completed but in a randomized order. To prevent rhythmic task structure from confounding neural activity and to discourage anticipatory or preparatory movements, trial timing was uniformly randomized. This resulted in an inter-trial interval of 1–1.5 s and a Go phase of 2.5–3.5 s during which movements were performed. This duration was sufficient for the participant to complete the instructed reach and gaze-shift behavior. If the movement was completed before the end of the Go phase, the participant briefly maintained their hand and gaze at the target locations until the trial ended.

The movement angle, from the center of the screen, was the primary behavioral metric used for both hand and eye movements. To verify the participant's correct execution of the task, eye movements were recorded with a 90 Hz binocular Tobii eye tracking system (Video S2), and hand movements were recorded using an external video camera (Video S3). These recordings were used to confirm that movements were performed in the instructed direction but were not used to extract detailed kinematic trajectories. Behavioral labels were instead defined by the instructed target locations presented during the task.

Neural signal recording and processing

Neural signals were recorded using the NeuroPort Neural Signal Processors (Blackrock Microsystems Inc.), then amplified, filtered with a bandpass range of 0.25–5 kHz, and digitized at 30 kHz with 16-bit resolution. Action potentials (spikes) were detected by applying a threshold set at −3.5 times the electrode's root-mean-square voltage. Single neurons were identified using the k-medoids clustering algorithm, with the optimal number of waveform clusters determined by the gap criterion. (Figure S7) Clustering was performed on a space comprised of principal components that collectively accounted for 95% of the waveform variance. Spike sorting was performed independently for each recording session. Neurons were not tracked across sessions; therefore, all isolated units were treated as independent session-specific neurons. Lastly, average FR is calculated as the number of spikes per second for each sorted single neuron. We use the FR instead of raw counts due to randomized trial lengths. Each neuron's activity is quantified as the average FR across the entire "Go" phase of the trial (2.5–3.5 s). Neurons with an average FR less than or equal to 1 Hz were excluded from the analysis.

Empirical tuning curves and surfaces

We represented neuron TCs nonparametrically. Let r_t be the FR on trial t. Let $X \in \{H,E\}$ be our two effector Hand and Eye, respectively. Let $C \in \{ME,SE\}$ be the two experimental contexts. For each effector, let $\theta_X \in \left\{\theta_X^{(1)},\ldots,\theta_X^{(6)}\right\}$ be the angles of the 6 targets and $b_X(t) \in \{1, \ldots,6\}$ be the target index for trial t. Let T_H^{SE}, T_E^{SE}, and T_{HE}^{ME} be the set of single effector hand, single effector eye, and multi-effector trials, respectively. We defined single effector TCs as

$$f_X^{SE}\left(\theta_X^{(k)}\right) = \frac{1}{\left|\left\{t \in \mathrm{T}_X^{SE} : b_X(t) = k\right\}\right|} \sum_{\substack{t \in \mathrm{T}_X^{SE} \\ b_X(t) = k}} r_t \,.$$

Similarly, we defined the multi-effector tuning surface as

$$f_{HE}^{ME}\left(\theta_H^{(i)},\theta_E^{(j)}\right) = \frac{1}{\left|\left\{t \in \mathrm{T}_{HE}^{ME} : b_H(t) = i, b_E(t) = j\right\}\right|} \sum_{\substack{t \in \mathrm{T}_{HE}^{ME} \\ b_H(t) = i \\ b_E(t) = j}} r_t \,.$$

These nonparametric forms allow us to compare the representations with raw data rather than models that approximate the data.

Additive separability is equivalent to zero cross-partial derivatives

Claim: A function is additively separable if and only if it has no cross-partial derivatives.

Proof:

(⇒) Additively separable ⇒ zero cross-partial.

If $f(\theta_H,\theta_E) = g(\theta_H) + h(\theta_E)$ then $f_{\theta_H}(\theta_H,\theta_E) = g'(\theta_H)$, and $f_{\theta_H\theta_E}(\theta_H,\theta_E) = \frac{\partial}{\partial\theta_E}g'(\theta_H) = 0$.

(⇐) Zero cross-partial ⇒ additively separable.

Assume, for all θ_H,θ_E,

$$f_{\theta_H\theta_E}(\theta_H,\theta_E) = \frac{\partial}{\partial\theta_E}\left(\frac{\partial}{\partial\theta_H}f(\theta_H,\theta_E)\right) = 0.$$

Therefore, $f_{\theta_H}(\theta_H,\theta_E)$ is independent of θ_E. Hence there exists a function $a(\theta_H)$ such that

$f_{\theta_H}(\theta_H,\theta_E) = a(\theta_H)$.

Integrating with respect to θ_H gives us.

$f(\theta_H,\theta_E) = \int a(\theta_H)\mathrm{d}\theta_H + h(\theta_E) = g(\theta_H) + h(\theta_E)$,

where the "constant of integration" h may depend on θ_E and $g(\theta_H) \equiv \int a(\theta_H)\mathrm{d}\theta_H$. Which, in turn, yields the equation for additive separability.

So,

$f_{\theta_H\theta_E}(\theta_H,\theta_E) = 0 \Leftrightarrow \mathrm{f}(\theta_\mathrm{H},\theta_E) = g(\theta_H) + h(\theta_E)$. **QED**

Separability calculations

A TS (function) is additively separable if and only if it has no cross-partial derivatives. Cross-partial derivatives are defined as

$$\frac{\partial^2 F(\theta_H,\theta_E)}{\partial\theta_H\partial\theta_E} = 0 \,.$$

This cross-partial derivative can be calculated numerically on the discrete grid using centered finite differences with circular wrap-around indexing in both angular dimensions. (see cross derivative finite difference).

TSs of neurons which are not mixed selective, are trivially additively separable because they are functions of only one variable. For example,

$$\frac{\partial^2 F(\theta_H)}{\partial\theta_H\partial\theta_E} = \frac{\partial}{\partial\theta_H}\left(\frac{\partial F(\theta_H)}{\partial\theta_E}\right) = \frac{\partial}{\partial\theta_H}(0) = 0\,.$$

Calculating the cross-derivative of neuron TSs is useful method when determining the interactions of variables in neural representations. This method benefits from naturally extending to systems with increasing numbers of effectors via the formalism of the Hessian matrix. The Hessian matrix quantifies the local curvature of a function by quantifying its second-order partial derivatives with respect to a pair of variables. A function (F) of two variables has a 2×2 Hessian matrix of the form

$$H(F(\theta_H,\theta_E)) = \nabla\bigotimes\nabla F(\theta_H,\theta_E) = \begin{bmatrix} \frac{\partial^2 F(\theta_H,\theta_E)}{\partial^2\theta_H} & \frac{\partial^2 F(\theta_H,\theta_E)}{\partial\theta_H\partial\theta_E} \\ \frac{\partial^2 F(\theta_H,\theta_E)}{\partial\theta_E\partial\theta_H} & \frac{\partial^2 F(\theta_H,\theta_E)}{\partial^2\theta_E} \end{bmatrix}.$$

In the context of neuronal representations, each element of a 2×2 Hessian reflects how sharply a neuron's FR changes with respect to hand and eye movements, either independently (diagonal terms) or jointly (off-diagonal terms). If a TS's Hessian is diagonal over its whole domain, it has no cross-partial derivatives and therefore is additively separable.

Additively separable functions have no cross terms. Therefore, additively separable TSs can be expressed as a simple sum of independent TCs

$$f_{HE}^{ME}(\theta_H,\theta_E) = g_H^{ME}(\theta_H) + h_E^{ME}(\theta_E)$$

where $g(\theta_H) = f_H^{ME}(\theta_H) - \bar{f}_H^{ME}$ is the centered hand TC averaged over all eye movements and $h(\theta_E) = f_E^{ME}(\theta_E) - \bar{f}_E^{ME} + c_{HE}^{ME}$ is the centered eye TC averaged over all hand movements plus the ME baseline activity (see projections and additive surfaces).

When calculating all of these cross-derivative quantities, biological noise and measurement error prevent values from being exactly zero. Therefore, cross-derivative values were measured as the root-mean-squared (rms) deviation (r_{RMS}; see root-mean-squared calculation) of cross-derivative of the TS from zero. These cross-derivative deviations could subsequently be compared to deviations arising from baseline noise.

Two pass smoothing

To reduce high-frequency sampling noise while preserving large-scale curvature structure, smoothing was applied twice sequentially:

$$\tilde{F}^{(2)} = \mathcal{S}(\mathcal{S}(F))$$

where $\mathcal{S}(\cdot)$ denotes the circular kernel smoothing operation (see Circular Kernel mean and variance).

This 2-pass procedure is equivalent to convolution with the kernel twice and results in a smoother effective kernel with reduced variance.

The identical 2-pass smoothing procedure was applied to both empirical and permuted TSs. Therefore, smoothing does not bias the permutation test (see separability permutation test), as both observed and null statistics are computed under the same estimator.

The rationale for this decision is that second derivatives scale like:

$$\partial^2 F \sim \frac{\Delta F}{\Delta\theta^2}$$

and thus amplify bin-level noise by a factor proportional to $1/\Delta\theta^2$. On a coarse 6-bin grid, this amplification is substantial. The 2-pass smoothing stabilizes derivative estimates while preserving meaningful curvature structure at the scale of behavioral sampling.

Cross Derivative Finite Difference

When testing additive separability, we quantified the cross-derivative energy of the multi-effector TS $f_{HE}^{ME}(\theta_H,\theta_E)$. On the discrete 6×6 grid, mixed partial derivatives were estimated using centered finite differences with circular wrap-around indexing in both angular dimensions.

Specifically, at grid point (h,e),

$$\left.\frac{\partial^2 f_{HE}^{ME}(\theta_H,\theta_E)}{\partial\theta_H\,\partial\theta_E}\right|_{(h,e)} \approx \frac{f_{HE}^{ME}(h+\Delta\theta_H, e+\Delta\theta_E) - f_{HE}^{ME}(h+\Delta\theta_H, e-\Delta\theta_E) - f_{HE}^{ME}(h-\Delta\theta_H, e+\Delta\theta_E) + f_{HE}^{ME}(h-\Delta\theta_H, e-\Delta\theta_E)}{4\,\Delta\theta_H\,\Delta\theta_E},$$

with uniform spacings $\Delta\theta_H$ and $\Delta\theta_E$.

For each neuron we summarized interaction strength by the root-mean-square Hz/rad^2 (see root-mean-squared calculation) across evaluated grid points from a zero reference. Since finite sampling noise ensures a nonzero baseline r_{RMS} even under true separability, we constructed a permutation-based null. For each neuron, FRs were randomly permuted (1000 times) across trials while preserving angular coordinates. The TS, its derivatives, and the RMS statistics were recomputed for each permutation to form a null distribution, and significance was assessed using a right-tailed permutation test. An FDR-BH adjustment was used due to repeated tests for each neuron. Positive test results implied neurons had significant cross-derivatives/variable interactions and negative results implied neurons were additively separable with no variable interactions.

Root-Mean-Squared Calculation

When comparing the deviation of cross-derivative surface from zero we used root-mean-squared as a metric. For each neuron we evaluated root-mean-square across all grid points,

$$RMS_{HE} = \sqrt{\frac{1}{M}\sum_{h,e}\left(\left.\frac{\partial^2 f_{HE}^{ME}(\theta_H,\theta_E)}{\partial\theta_H\,\partial\theta_E}\right|_{(h,e)}\right)^2},$$

where M is the number of points included.

Projections and Additive Surfaces

Additive separability enables the transformation of ME TSs into ME TCs as well as the combination of SE TCs into SE TSs. Projections of separable ME TSs onto individual variables are

$$f_H^{ME}(\theta_H) = \langle f_{HE}^{ME}(\theta_H,\theta_E)\rangle_{\theta_E}, f_E^{ME}(\theta_E) = \langle f_{HE}^{ME}(\theta_H,\theta_E)\rangle_{\theta_H},$$

where the symbol $\langle\cdot\rangle$ denotes averaging across the variable's bins. Centered versions of these projections

$$g(\theta_{\mathrm{H}}) = f_H^{ME}(\theta_{\mathrm{H}}) - \bar{f}_H^{ME}, h(\theta_{\mathrm{E}}) = f_E^{ME}(\theta_{\mathrm{E}}) - \bar{f}_E^{ME} + c_{HE}^{ME}$$

can be understood as TCs of each variable in the ME context, where $\bar{f}_H^{ME} = \langle f_H^{ME}(\theta_H)\rangle_{\theta_H}$ and $\bar{f}_E^{ME} = \langle f_E^{ME}(\theta_E)\rangle_{\theta_E}$ are the means (baseline FRs) of the projections. The constant c_{HE}^{ME} is the grand mean of TS $\langle f_{HE}^{ME}(\theta_H,\theta_E)\rangle_{\theta_H,\theta_E}$. Centering TCs prevents double-counting the baseline FRs and the offset c_{HE}^{ME} restores the baseline appropriate to the context being modeled.

These ME TCs can now be easily compared to their SE TCs counter parts using representational similarity metrics (see representation similarity metrics). However, using our equation for additive separability

$$f_{HE}^{ME}(\theta_{\mathrm{H}},\theta_{\mathrm{E}}) = g_H^{ME}(\theta_{\mathrm{H}}) + h_E^{ME}(\theta_{\mathrm{E}})$$

we can reconstruct ME TSs from our projection based ME TCs without loss of information. Such reconstructed ME surfaces take the form

$$\hat{f}_{HE}^{ME}(\theta_H,\theta_E) = f_H^{ME}(\theta_H) - \bar{f}_H^{ME} + f_E^{ME}(\theta_E) - \bar{f}_E^{ME} + c_{HE}^{ME}.$$

Similar to the reconstructed ME TS, raw empirical SE TCs can also be composed into additively compositional TSs as

$$\hat{f}_{HE}^{SE}(\theta_{\mathrm{H}},\theta_{\mathrm{E}}) = f_H^{SE}(\theta_{\mathrm{H}}) - \bar{f}_H^{SE} + f_E^{SE}(\theta_{\mathrm{E}}) - \bar{f}_E^{SE} + c_{HE}^{SE},$$

where f_H^{SE} and f_E^{SE} are the SE TCs, $\bar{f}_H^{SE} = \langle f_H^{SE}(\theta_H)\rangle_{\theta_H}$ and $\bar{f}_E^{SE} = \langle f_E^{SE}(\theta_E)\rangle_{\theta_E}$ are their means, and c_{HE}^{SE} is the predicted mean of the SE TS determined using a weighted average of $\bar{f}_H^{SE}$ and $\bar{f}_E^{SE}$ (see weighted SE baseline). Centering of the TCs ($f_H^{SE}(\theta_{\mathrm{H}})$ and $f_E^{SE}(\theta_{\mathrm{E}})$) prevents double-counting the baseline FR and the offset c_{HE}^{SE} restores the baseline appropriate to the context being modeled. This SE TS allows for comparison of ME TSs with new TSs as predicted purely from SE TCs.

Residual surfaces

When characterizing inseparable neurons, it is helpful to analyze the residual surface after subtracting the additive components. The additive component of the surface is

$$\hat{f}_{HE}^{ME}(\theta_H,\theta_E) = f_H^{ME}(\theta_H) - \bar{f}_H^{ME} + f_E^{ME}(\theta_E) - \bar{f}_E^{ME} + c_{HE}^{ME}.$$

Subtracting this additive component from the raw empirical surface leaves you with the residual ME surface written as

$$R = f_{HE}^{ME}(\theta_{\mathrm{H}},\theta_{\mathrm{E}}) - \hat{f}_{HE}^{ME}(\theta_{\mathrm{H}},\theta_{\mathrm{E}}).$$

For inseparable neurons, the residual surface represents the component of the joint hand-eye response that is not explained by the additive hand and eye marginal effects.

Representation Similarity Metrics

Equipped with TSs and curves in both contexts ({*ME*,*SE*}) we can compare representations with a couple key metrics. Firstly, the preferred direction (PD) for an effector $X \in \{H,E\}$ and context $C \in \{ME,SE\}$ is the bin of maximal mean response,

$$\mathrm{PD}_X^C = arg\ \max_{\theta_X} f_X^C(\theta_X)\ .$$

Another important metric is the amplitude of a TC as the difference in FR between the peak and trough of the TC:

$$A_X^C = \max_{\theta_X} f_X^C(\theta_X) - \min_{\theta_X} f_X^C(\theta_X),$$

where $f_X^C(\theta_X)$ is the TC for each effector X and each context C. Figure 3A illustrates this definition for the ME data using a light gray segment that is centered at $\widehat{\theta}_X^{ME}$ and spans A_X^{ME}. However, the two contexts in C have different numbers of trials. The fewer number of points used to calculate the TC in the SE context increases the amplitude variance. To account for such differences, we z-scored the TC amplitudes using a permutation-based amplitude null distribution,

$$Z_X^C = \frac{A_X^C - \mu_{X,0}^C}{\sigma_{X,0}^C},$$

with $\mu_{X,0}$ and $\sigma_{X,0}$ being the mean and standard deviation of the amplitude null distribution $\left\{A_{X,s}^C\right\}_{s=1}^{500}$. The amplitude null distribution was created by shuffling trial labels (independently for hand and eye) and recomputing the six-bin TC. Each shuffle (s) creates permuted amplitude $A_{X,s}^C$ that is used in the null distribution.

Weighted SE baseline

Our results demonstrated that ME TSs had baselines most similar to the baselines of the dominantly encoded effector. This inspired the use of a weighted SE baseline that could predict the baseline of the ME TS from SE TCs. This weighted baseline FR was defined as

$$c_{HE}^{SE} = \frac{A_H^{SE}}{A_H^{SE}+A_E^{SE}}\bar{f}_H^{SE} + \frac{A_E^{SE}}{A_H^{SE}+A_E^{SE}}\bar{f}_E^{SE},$$

where A_X^{SE} and $\bar{f}_X^{SE}$ are the neurons' tuning curves' amplitudes and means, respectively.

Proof of population separability

In this paper we claim that if single neurons are additively separable then linear combinations (linear projections) of those neurons are also additively separable.

Claim: If $f_{HE,k}^C(\theta_H,\theta_E)$ is additively separable $\forall k \in \{1,\ldots,N\}$ then a linear projection of the population $g_{HE}^C(\theta_H,\theta_E)$ is also additively separable.

Proof 1: Let us define a linear combination of neurons as,

$g_{HE}^C(\theta_H,\theta_E) := \sum_{k=1}^N w_k f_{HE,k}^C(\theta_H,\theta_E)$.

Assuming additive separability of the neurons,

$f_{HE,k}^C(\theta_H,\theta_E) = f_{H,k}^C(\theta_H) - \bar{f}_{H,k}^C + f_{E,k}^C(\theta_E) - \bar{f}_{E,k}^C + c_{HE,k}^C$.

We can then plug this definition of $f_{HE,k}^C(\theta_H,\theta_E)$ into the linear combination and distribute such that

$g_{HE}^C(\theta_H,\theta_E) = \sum_{k=1}^N w_k\left[f_{H,k}^C(\theta_H) - \bar{f}_{H,k}^C\right] + \sum_{k=1}^N w_k\left[f_{E,k}^C(\theta_E) - \bar{f}_{E,k}^C\right] + \sum_{k=1}^N w_k c_{HE,k}^C$.

Observing the structure we can simplify each sum on the RHS such that.

$g_{HE}^C(\theta_H,\theta_E) = g_H^C(\theta_H) + g_E^C(\theta_E) + C$,

which is additive separability of the linear combination by definition. **QED**.

Proof 2: Let us define a linear combination of neurons as,

$g_{HE}^C(\theta_H,\theta_E) := \sum_{k=1}^N w_k f_{HE,k}^C(\theta_H,\theta_E)$.

By linearity of differentiation,

$$\frac{\partial^2}{\partial\theta_H\partial\theta_E} g_{HE}^C(\theta_H,\theta_E) = \sum_{k=1}^N w_k\left[\frac{\partial^2}{\partial\theta_H\partial\theta_E} f_{HE,k}^C(\theta_H,\theta_E)\right].$$

Assuming $f_{HE,k}^C(\theta_H,\theta_E)$ are additively separable, we know their cross derivative is zero. Therefore

$\frac{\partial^2}{\partial\theta_H\partial\theta_E} g_{HE}^C(\theta_H,\theta_E) = \sum_{k=1}^N w_k \cdot 0 = 0$.

Thus g satisfies the necessary and sufficient condition for additive separability. **QED**.

Circular Kernel Mean and Variance

When estimating likelihoods based on nonparametric tuning representations the simplest approach is to compute per-bin means, treating each bin across the curve or grid as independent categories. However, this approach leaves out useful information about the relationship between points. TCs should be continuous, so using information from adjacent bins to smooth, improves bin mean estimates. To do this we standardized the per-neuron FRs and used a kernel-based smoothing estimator. We used a von Mises kernel (K) to respect circular geometry, which can be written as

$$K_X(\Delta_X) = e^{\kappa_X \cos \Delta_X},$$

where $\Delta_{X,t} = d(\theta_X,\theta_{X,t})$ is a wrapped angular difference and κ_X is concentration (bandwidth) controlling smoothness. (small κ = more smoothing; large κ = less smoothing) Next, we did 2D or 1D Nadaraya–Watson smoothing,[50–52]

$$\widehat{\mu}^{ME}_{HE,n}(\theta_H,\theta_E) = \frac{\sum_{t\in T^{ME}_{HE}} K_H(\Delta_{H,t})\, K_E(\Delta_{E,t})\, r_{t,n}}{\sum_{t\in T^{ME}_{HE}} K_H(\Delta_{H,t})\, K_E(\Delta_{E,t})}, \widehat{\mu}^{SE}_{X,n}(\theta_X) = \frac{\sum_{t\in T^{SE}_{X}} K_X(\Delta_{X,t})\, r_{t,n}}{\sum_{t\in T^{SE}_{X}} K_X(\Delta_{X,t})}.$$

The bandwidth κ was chosen per neuron by 5-fold cross-validation on the training trials (CV) to minimize the Gaussian negative log likelihood

$$\kappa_n = \arg\min_{\kappa\in\mathcal{K}} \mathcal{L}_n(\kappa),$$

where $\mathcal{K} = \{2,4,8,12,\ldots,32\}$ and

$$\mathcal{L}_n(\kappa) = \sum_{t\in CV} -\log\left(p\left(r_{t,n}\middle|\theta_{H,t},\theta_{E,t};\kappa\right)\right).$$

The likelihood $p\left(r_{ref,n}\middle|\theta_H,\theta_E\right)$ is defined below (see Bayesian inference).

When adding the tuning curves together we again did the following:

$$\widehat{\mu}^{SE}_{HE,n}(\theta_H,\theta_E) = \left(\widehat{\mu}^{SE}_{H,n}(\theta_H) - \overline{\widehat{\mu}^{SE}_{H,n}}\right) + \left(\widehat{\mu}^{SE}_{E,n}(\theta_E) - \overline{\widehat{\mu}^{SE}_{E,n}}\right) + c^{SE}_{HE}.$$

We accompany the mean value calculations with predictive noise models. For the ME surface we calculated global variance as well as local heteroskedastic variance using kernel weights. We define these variance calculation as

$$\widehat{\sigma}^{ME}_{HE,n,loc}(\theta_H,\theta_E)^2 = \frac{\sum_{t\in T^{ME}_{HE}} K_H(\Delta_{H,t})\, K_E(\Delta_{E,t})\left(r_{t,n} - \widehat{\mu}^{ME}_{HE,n}(\theta_H,\theta_E)\right)^2}{\sum_{t\in T^{ME}_{HE}} K_H(\Delta_{H,t})\, K_E(\Delta_{E,t})}, \quad \left(\widehat{\sigma}^{ME}_{HE,n,glob}\right) = \frac{\sum_{t\in T^{ME}_{HE}}\left(r_{t,n} - \widehat{\mu}^{ME}_{HE,n}(\theta_{H,t},\theta_{E,t})\right)^2}{\left\|\{T^{ME}_{HE}\}\right\|}^2.$$

To provide conservative regularization we also perform shrinkage toward each neuron's global variance

$$\widehat{\sigma}^{ME}_{HE,n}(\theta_H,\theta_E)^2 = \tau\left(\widehat{\sigma}^{ME}_{HE,n,glob}\right)^2 + (1-\tau)\,\widehat{\sigma}^{ME}_{HE,n,loc}(\theta_H,\theta_E)^2,$$

with $0 \le \tau \le 1$ (we used $\tau = 0.3$). Alternatively, for the SE surfaces we kept the variance calculations independent and simply added them as we did with the means. To assess variance for each independent effector, we calculated

$$\widehat{\sigma}^{SE}_{X,n,loc}(\theta_X)^2 = \frac{\sum_{t\in T^{SE}_{X}} K_X(\Delta_{X,t})\left(r_{t,n} - \widehat{\mu}^{SE}_{X,n}(\theta_X)\right)^2}{\sum_{t\in T^{SE}_{X}} K_X(\Delta_{X,t})},$$

$$\left(\widehat{\sigma}^{SE}_{X,n,glob}\right)^2 = \frac{\sum_{t\in T^{SE}_{X}}\left(r_{t,n} - \widehat{\mu}^{SE}_{X,n}(\theta_{X,t})\right)^2}{\left\|\{T^{SE}_{X}\}\right\|}.$$

After calculating the variance independently, we also performed shrinkage

$$\widehat{\sigma}^{SE}_{X,n}(\theta_X)^2 = \tau\left(\widehat{\sigma}^{SE}_{X,n,glob}\right)^2 + (1-\tau)\,\widehat{\sigma}^{SE}_{X,n,loc}(\theta_X)^2,$$

toward each variable's global variance, separately (again we used $\tau = 0.3$). We then calculated SE surface variance by adding the independent variance values

$$\widehat{\sigma}^{SE}_{HE,n}(\theta_H,\theta_E)^2 = \widehat{\sigma}^{SE}_{H,n}(\theta_H)^2 + \widehat{\sigma}^{SE}_{E,n}(\theta_E)^2$$

as we did with the mean values. The mean and variance values calculated here are used to specify Gaussian likelihoods used for stimulus inference.

Bayesian Inference

For a single neuron, a TS, given any test trial $t \in T^{ME}_{HE,test}$ with observed firing vector $r_{t,n}$, can be turned into a likelihood

$$p\left(r_{ref,n}\middle|\theta_H,\theta_E\right) = \mathcal{N}\left(r_{ref,n};\widehat{\mu}^{C}_{HE,n}(\theta_H,\theta_E),\widehat{\sigma}^{C}_{HE,n}(\theta_H,\theta_E)^2\right) = \frac{1}{\sqrt{2\pi\,\widehat{\sigma}^{C}_{HE,n}(\theta_H,\theta_E)^2}}\,e^{\left(-\frac{\left(r_{ref,n}-\widehat{\mu}^{C}_{HE,n}(\theta_H,\theta_E)\right)^2}{2\,\widehat{\sigma}^{C}_{HE,n}(\theta_H,\theta_E)^2}\right)}.$$

However, we recorded from many neurons that all respond to these movement stimuli. If we assume that neuron responds roughly independently to a given stimulus the population likelihood becomes

$$p\left(r_{ref,1},\ldots,r_{ref,N}\middle|\theta_H,\theta_E\right) = \prod_{n=1}^{N} p\left(r_{ref,n}\middle|\theta_H,\theta_E\right).$$

Using Bayes' equation for inference,

$$p\left(\theta_H,\theta_E\middle|r_{ref,1},\ldots,r_{ref,N}\right) = \frac{\prod_{n=1}^{N} p\left(r_{ref,n}\middle|\theta_H,\theta_E\right)p(\theta_H,\theta_E)}{p\left(r_{ref,1},\ldots,r_{ref,N}\right)}.$$

Assuming a uniform prior on movement directions and dropping the marginal distribution for FRs as a proportionality constant the posterior is proportional to the likelihood,

$$p\left(\theta_H,\theta_E\middle|r_{ref,1},\ldots,r_{ref,N}\right) \propto \prod_{n=1}^{N} p\left(r_{ref,n}\middle|\theta_H,\theta_E\right) \propto \prod_{n=1}^{N} \frac{1}{\sqrt{2\pi\,\widehat{\sigma}^{C}_{HE,n}(\theta_H,\theta_E)^2}}\,e^{\left(-\frac{\left(r_{ref,n}-\widehat{\mu}^{C}_{HE,n}(\theta_H,\theta_E)\right)^2}{2\,\widehat{\sigma}^{C}_{HE,n}(\theta_H,\theta_E)^2}\right)}.$$

Using this population posterior we performed a maximum a posteriori (MAP) estimate of θ_H & θ_E given observed population FRs to $r_{ref,1}, \ldots, r_{ref,N}$. Because of assuming a uniform prior this map estimate was equivalent to a maximum likelihood estimate (MLE). Thus, we equivalently calculated,

$$\log p\left(\theta_H,\theta_E\middle|r_{ref,1},\ldots,r_{ref,N}\right) = \sum_{n=1}^{N} \log \mathcal{N}\left(r_{ref,n};\widehat{\mu}^{C}_{HE,n}(\theta_H,\theta_E),\widehat{\sigma}^{C}_{HE,n}(\theta_H,\theta_E)^2\right).$$

We evaluated $\arg\max_{\theta\in\Theta} logp\left(\theta_H,\theta_E\middle|r_{1,ref},\ldots,r_{N,ref}\right)$ on all 36 states of Θ and returned $\widehat{\theta}_{H,t}$ & $\widehat{\theta}_{E,t}$.

Inverted dropping curve

To characterize how decoding performance scaled with population size, we constructed inverted dropping curves within each recording session. For each session containing N simultaneously recorded neurons, decoding accuracy was evaluated as a function of the number of neurons included in the model.

For a given population size $x \in \{1, \ldots, N\}$, neurons were randomly sampled without replacement from the available pool within that session. For each sampled subset, the decoder was trained and evaluated on the test set. Decoding accuracy was computed as the proportion of correctly classified trials. This procedure was repeated multiple times for each x (with independent random subsets) to reduce sampling variance.

To visualize overall scaling trends across sessions, accuracy values for each sampled subset were pooled across sessions, yielding a set of points $\{(x,y)\}$. No cross-session normalization of neuron count was applied; instead, curves were evaluated up to the maximum available neuron count in each session.

To summarize the scaling relationship and estimate asymptotic performance, pooled accuracy values were fit with a saturating exponential model of the form

$$\widehat{y}(x) = L - (L - y_0)\,e^{-kx},$$

where x is the number of neurons, y_0 is the fitted intercept at $x = 0$, $L > 0$ represents the asymptotic performance limit, $k > 0$ controls the rate of saturation.

Parameters y_0, L, and k were estimated using least squares. For visualization purposes, exponentials were extrapolated beyond the maximum observed population size using the fitted parameters.

QUANTIFICATION AND STATISTICAL ANALYSIS

All statistical analyses were performed using custom scripts in MATLAB, and all tests were two-sided unless otherwise noted.

Weighted coefficient of determination

To quantify reconstruction quality across neurons, we compared f_{HE}^{ME} and $\hat{f}_{HE}^{ME}$ over the common 6 × 6 grid using a weighted coefficient of determination,

$$R^2 = 1 - \frac{\sum_i w_i \left(r_i - \hat{r}_{add,i}^{ME}\right)^2}{\sum_i w_i \left(r_i - \mu\right)^2}, \mu = \frac{\sum_i w_i r_i}{\sum_i w_i},$$

where i indexes H-E bin pairs and wi can equal the number of trials contributing to cell i (or wi ≡ 1 when coverage is uniform). Weighting guarded against spuriously penalizing sparsely sampled bins.

Separability Permutation Test

To assess statistical significance of RMS deviation, we constructed a permutation-based null distribution separately for each neuron. Within each neuron FRs were randomly permuted across trials to create a random ME surface. Subsequently the RMS cross-derivative value was recalculated based on the random ME surface. The random surface, as well as the observed surface, were subject to two pass smoothing to reduce second derivative noise during this test (see two pass smoothing). This process was repeated many times (N = 1000 permutations), yielding a neuron-specific null distribution:

$$\left\{RMS_{HE}^{(k)}\right\}_{k=1}^{N}$$

This null preserves the empirical firing-rate distribution and sampling density of each grid bin but destroys any systematic dependence on hand and eye angle.

Then, for each neuron, a one-sided p-value was computed as

$$p = \frac{\#\left\{\mathrm{RMS}_{HE}^{(k)} \geq \mathrm{RMS}_{HE}^{\mathrm{obs}}\right\}}{N}$$

reflecting the probability that a random surface would exhibit interaction curvature at least as large as the observed value.

Because separability was tested across large neuronal populations, we controlled the false discovery rate (FDR) at $q < 0.05$ using the Benjamini–Hochberg procedure. Resulting q-values were used for all statistical inferences.

Selectivity permutation tests and bootstrapping

Permutation tests were also used to determine the statistical significance of effector-specific tuning (selectivity) based on the representation metrics (see representation similarity metrics). All statistical procedures were fully nonparametric to accommodate heteroskedastic and non-Gaussian firing-rate distributions.

To quantify modulation of a neuron's FR by a given effector, we defined the z-scored tuning amplitude Z_X^C, where $X \in \{H,E\}$ denotes hand or eye and C denotes the experimental context (single-effector or ME). Tuning amplitude was computed as the range of the TC across target angles, normalized by the standard deviation of FRs across trials.

To assess whether observed tuning exceeded chance levels, we employed a nonparametric, permutation-based statistical test. For each neuron and condition, we generated a null distribution $Z_{X,0}^C$ by randomly permuting trial labels across target-angle bins, thereby preserving the marginal firing-rate distribution while destroying any systematic relationship between FR and movement direction. A one-sided p-value was then computed as

$$p_X^C = \Pr\left(Z_{X,0}^C \geq Z_X^C\right),$$

corresponding to the probability that a neuron drawn from the null distribution exhibited tuning amplitude greater than or equal to the observed value.

Because significance testing was performed across large neuronal populations, we controlled the false discovery rate (FDR) at α = 0.05 using the Benjamini–Hochberg procedure. Each family of p-values (ME-H, ME-E, SE-H, SE-E) was converted into q-values q_X^C, which were used for all selectivity assignments.

During initial analyses, we found that increasing the number of permutations alone did not yield stable q-values across different random seeds, particularly for neurons near threshold. To improve robustness, we therefore embedded the permutation test within

a bootstrap procedure. Specifically, we generated $B = 500$ bootstrap resamples by sampling trials with replacement within each condition. For each bootstrap resample b, we recomputed the tuning amplitude $Z^C_{X,b}$, corresponding null distribution, and FDR-corrected q-value $q^C_{X,b}$.

This procedure produced a distribution of q-values $\left\{q^C_{X,b}\right\}_{b=1}^{B}$ and effect sizes $\left\{Z^C_{X,b}\right\}_{b=1}^{B}$. We defined the median q-value

$$q^C_{X,\mathrm{med}} = \mathrm{median}_b\left(q^C_{X,b}\right)$$

as our final significance metric, and the median tuning amplitude

$$Z^C_{X,\mathrm{med}} = \mathrm{median}_b\left(Z^C_{X,b}\right)$$

as the corresponding effect size.

Neurons were classified as hand-selective if $q^C_{H,\mathrm{med}} < \alpha$, eye-selective if $q^C_{E,\mathrm{med}} < \alpha$, both-selective (mixed-selective) if both were significant, and none-selective otherwise.

ADDITIONAL RESOURCES

This research is part of a human brain-machine interface clinical trial (NCT01958086): https://clinicaltrials.gov/study/NCT01958086?term=NCT01958086&rank=1.

Cell Reports, Volume *45*

Supplemental information

The compositional encoding of hand-eye coordinated movements for single neurons in the posterior parietal cortex

Nikos A. Mynhier, Jorge Gamez, Kellan P. Moorse, Kelsie Pejsa, Ausaf Bari, Richard M. Murray, and Richard A. Andersen

FIGURE S1

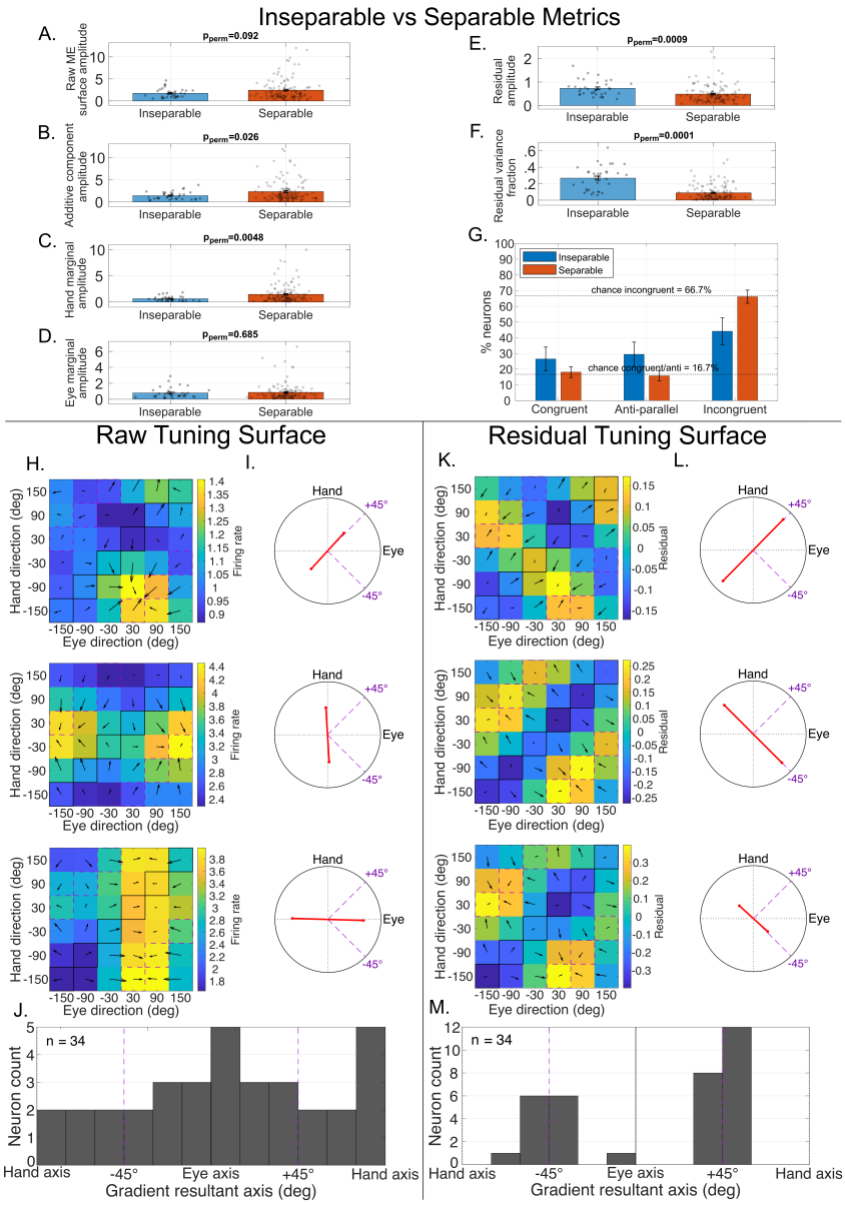


Figure S1. Structure of inseparable SPL neurons and their residual interaction components.
(A–F) Comparison of tuning-surface metrics between inseparable (n = 34) and separable (n = 127) SPL neurons. (A) Raw multi-effector (ME) tuning-surface amplitude. (B) Additive-component amplitude obtained from the separable reconstruction. (C) Hand marginal tuning amplitude. (D) Eye marginal tuning amplitude. (E) Residual interaction-component amplitude after subtracting the additive reconstruction from the raw ME tuning surface. (F) Residual variance fraction, defined as the fraction of tuning-surface variance explained by the residual interaction component. For panels (A–F), points indicate values for individual neurons, bars indicate distribution means ± SEM, and p-values are from two-sided permutation tests comparing means between inseparable and separable neurons. (G) Distribution of residual interaction peak locations, classified as congruent, anti-parallel, or incongruent hand–eye target combinations. Bars show the percentage of neurons in each category ± binomial SEM. Dashed lines indicate the expected proportions under a uniform distribution of peak locations. (H) Example raw ME tuning surfaces from 3 representative inseparable SPL neurons. Heatmaps show firing rate as a function of hand and eye target location. Arrows indicate the local gradient field. Black outlines indicate congruent hand–eye target combinations and magenta dashed outlines indicate anti-parallel target combinations. (I) Principal orientation of the gradient field corresponding to the example raw tuning surfaces shown in (H). Red bars indicate the estimated axis angle and strength, computed as $\boldsymbol{\theta} = \frac{1}{2}\boldsymbol{arg}\left(\sum_i \boldsymbol{w_i e^{2i\phi_i}}\right)$; $\boldsymbol{R} = \frac{\left|\sum_i w_i e^{2i\phi_i}\right|}{\sum_i w_i}$, respectively. (J) Distribution of principal axes for the raw tuning surfaces of all inseparable SPL neurons. (K) Residual interaction surfaces corresponding to the same 3 example neurons shown in (H), obtained after subtracting the additive reconstruction from the raw ME tuning surface. Heatmaps show residual firing-rate modulation and arrows indicate the local residual gradient field. (L) Principal axes corresponding to the residual surfaces shown in (K). Red bars indicate the principal axis angle and strength for each of the residual surfaces. (M) Distribution of principal axes of the residual surfaces for all inseparable SPL neurons.

FIGURE S2

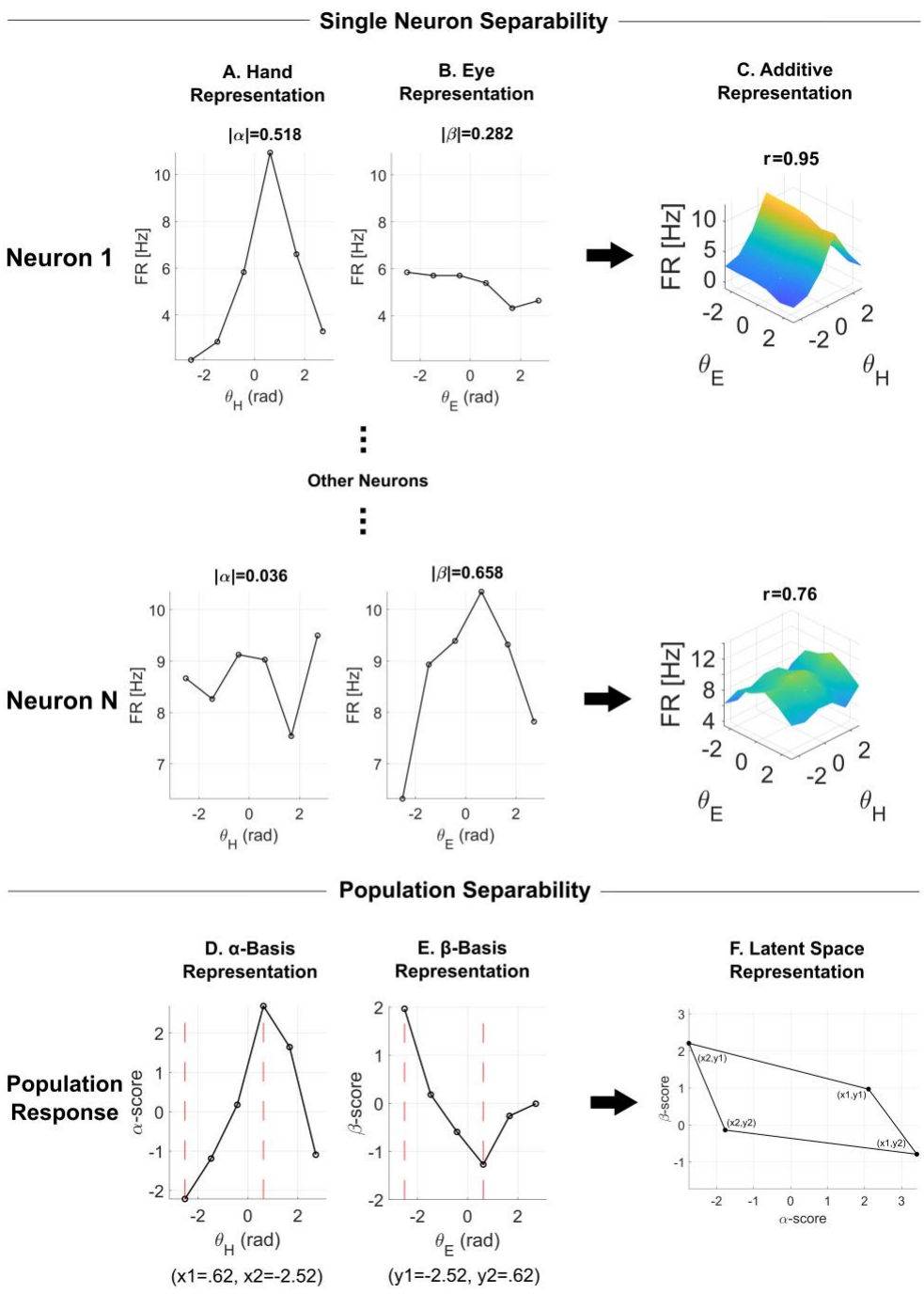


Figure S2. Single-neuron and population additivity tested with a demixed additive basis (DAB).
All data presented here are taken from a single representative clinical session. (A–C) Single neuron activity. For each neuron, we computed mean firing rates on a (6x6) hand–eye grid and tested additive separability. (A) Projected ME hand tuning curves of single neurons. (B) Projected ME eye tuning curves of single neurons. The neurons' absolute DAB loadings ($|\alpha_n|$) and ($|\beta_n|$) are reported above the tuning curves. (C) Additive ME surface ($\hat{f}^{ME}_{HE}(\theta_H, \theta_E)$). The correlation between the additive surface and the raw ME surface ($corr(f^{ME}_{HE}, \hat{f}^{ME}_{HE})$) is shown above each additive surface.
(D–F) Population activity. Demixed additive basis vectors $\{\alpha,\beta\} \subset R^N$, representing linear combinations of all neuronal activity, were constructed by applying SVD to the population hand and eye marginals. (D) α-basis score vs hand direction (averaged across eye directions). (E) β-basis score vs eye direction. Vertical red lines mark the peak and trough of panel D (x1,x2) and panel E (y1,y2). (F) Four projected points, $\{s(x_i,y_j), t(x_i,y_j)\}$ for $(x_i, y_j) \in \{x1, x2\} \times \{y1, y2\}$, shown in the population latent space; these points form a parallelogram.

FIGURE S3

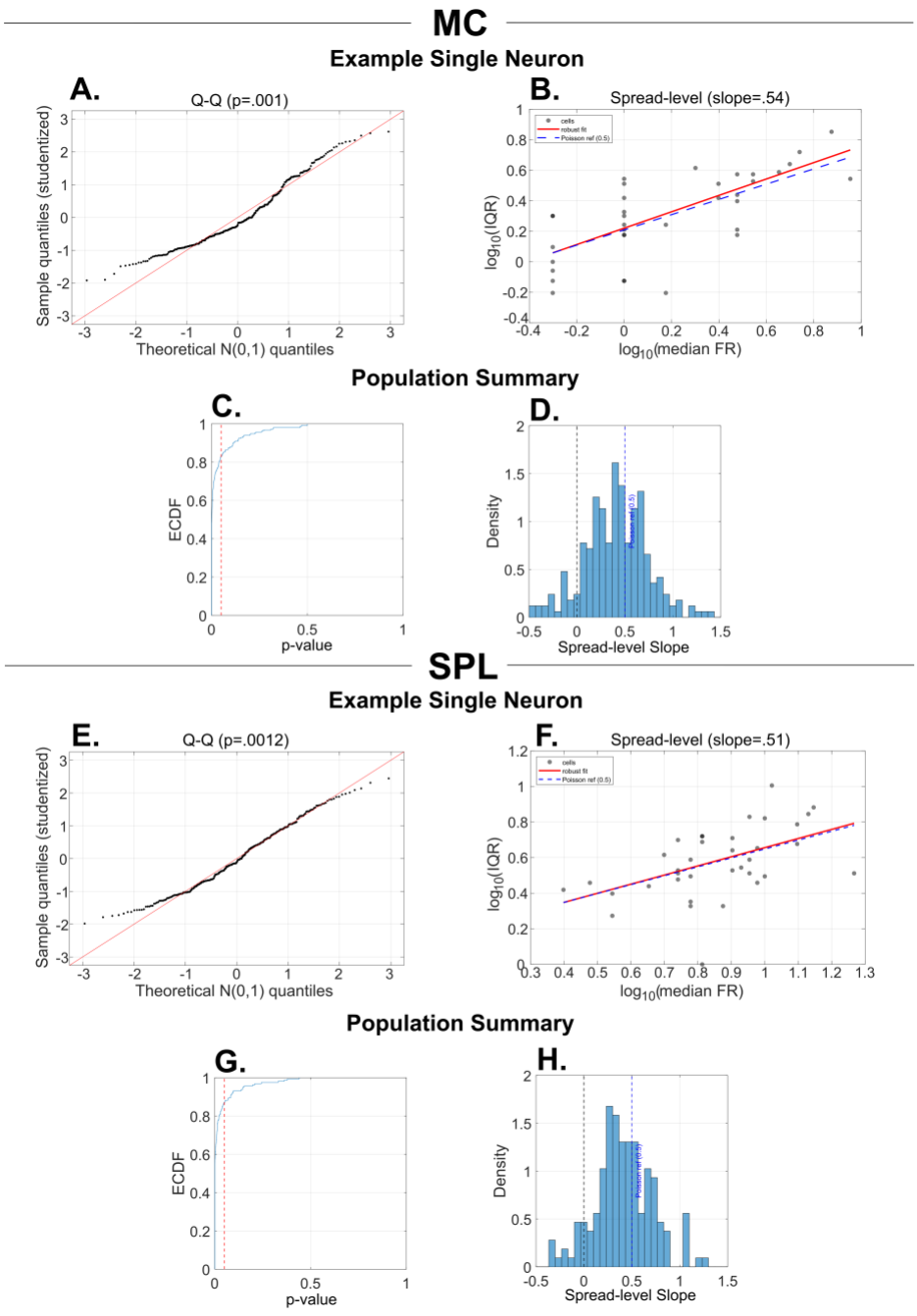


Figure S3. Non-normality and heteroskedasticity of single neurons in MC and SPL

Panels A–D show results for the MC and panels E–H show results for the SPL. For each brain area, the top two plots represent single-neuron results and the bottom two plots represent population-level results. (A) Q–Q plots of studentized residuals of an example neuron against an N(0,1) reference (red line). Residuals are defined trial-wise as $z_{ijt} = (r_{ijt} - \bar{r}_{ij})/s_{ij}$, where $\bar{r}_{ij}$ and s_{ij} are the mean and SD within each hand–eye combination (i, j). Clear curvature/tail excess indicates non-Gaussian errors even after within-cell scaling. The reported p-value is from a Lilliefors test on the pooled studentized residuals. (B) Spread–level plot for an example neuron. $log_{10}(IQR_{ij})$ versus $log_{10}(median_{ij})$ for each hand-eye combination (i, j). The solid line is a least squares linear fit to the scattered data. The blue dashed line represents mean-variance ratio (slope=0.5) of a Poisson process ($\sigma \propto \mu^{1/2}$). Positive slopes in general indicate heteroskedasticity. (C) ECDF of Lilliefors p-values across all neurons in the MC. The vertical dashed line marks p=0.05. Neurons with p-values less than 0.05 are significantly different from a normal distribution. (D) Histogram of spread–level slopes for all neurons in the MC. The dotted vertical lines mark 0 (no mean–variance relation) and 0.5 (Poisson mean-variance relation). Distributions centered above zero indicate heteroskedasticity. (E-H) Same plots as A-D but for neurons in the SPL.

FIGURE S4

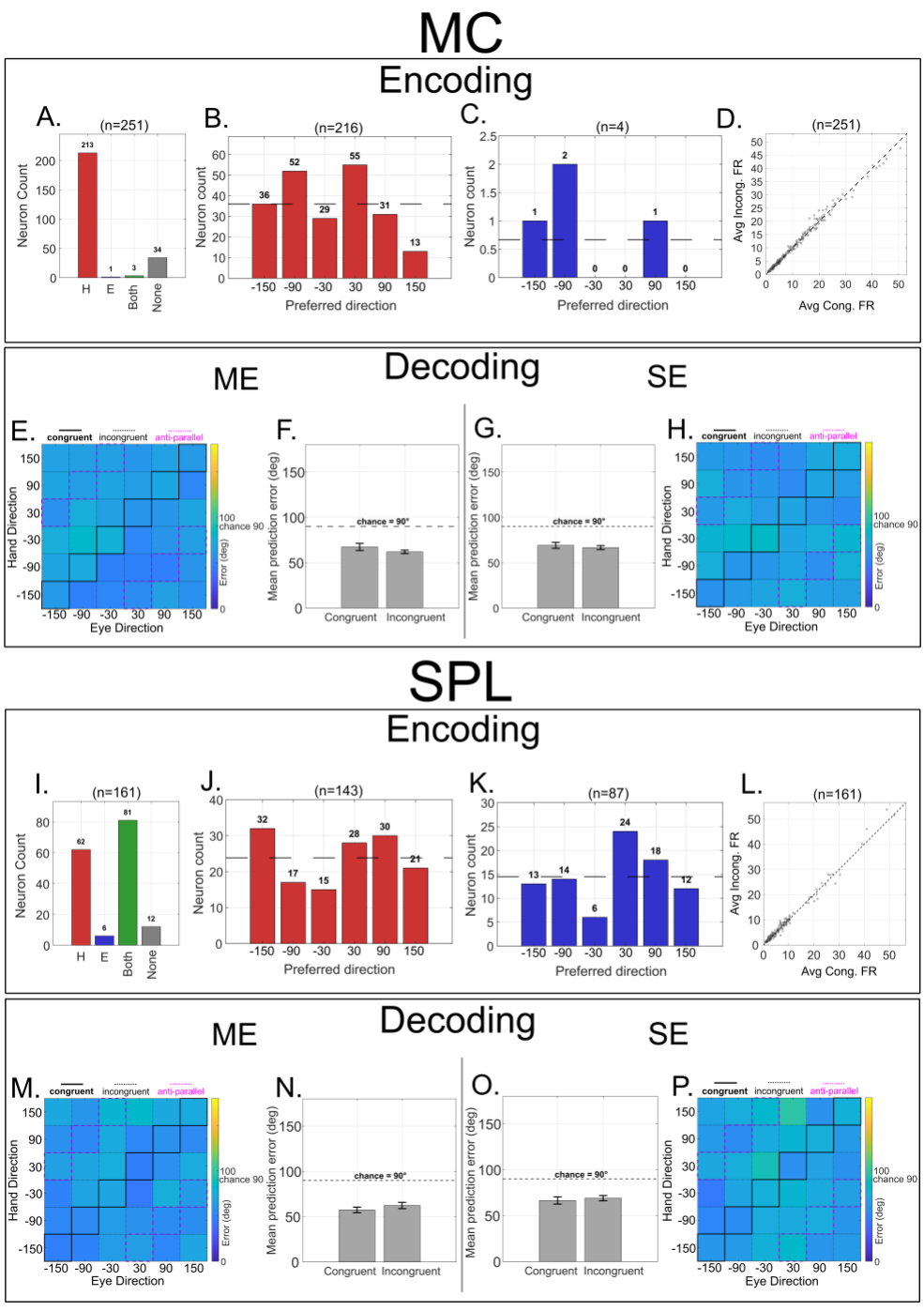


Figure S4. Neural activity and decoding performance during congruent and incongruent hand–eye movements.
(A–D) MC encoding analyses. (A) Selectivity classification of MC neurons into hand-selective (H), eye-selective (E), mixed-selective (Both), and non-selective (None) categories. (B) Distribution of preferred directions for hand-selective and mixed-selective MC neurons. (C) Distribution of preferred directions for eye-selective and mixed-selective MC neurons. (D) Comparison of average firing rates during congruent and incongruent hand–eye movement trials for all MC neurons. Each point represents one neuron, and the dashed line indicates equality. (E–H) MC decoding analyses. (E) Mean prediction error of the ME decoder for each hand–eye target combination. Black outlines indicate congruent target combinations and magenta dashed outlines indicate anti-parallel target combinations. (F) Mean (± SEM) ME decoding error for congruent and incongruent movement conditions. (G) Mean (± SEM) SE-compositional decoding error for congruent and incongruent movement conditions. (H) Mean prediction error of the SE-compositional decoder for each hand–eye target combination. (I–L) Same encoding analyses but for SPL. (M–P) Same decoding analyses but for SPL.

FIGURE S5

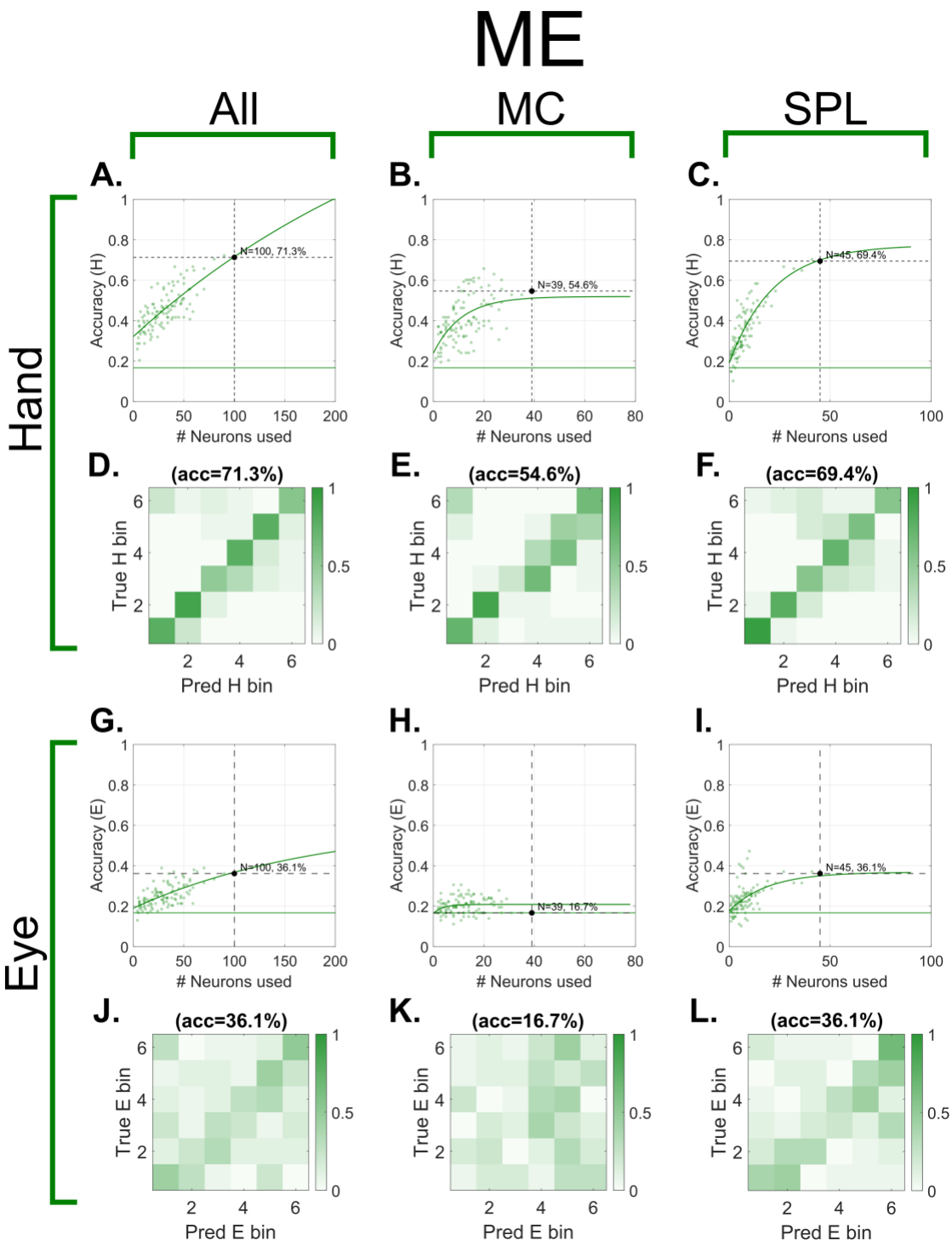


Figure S5. ME decoding using combined and region-specific neural populations.
ME decoding of coordinated hand–eye trials using neurons from the combined MC and SPL population (All), MC alone, or SPL alone. (A–C) Hand-decoding accuracy as a function of neuron count. (D–F) Hand-decoding confusion matrices. (G–I) Eye-decoding accuracy as a function of neuron count. (J–L) Eye-decoding confusion matrices. Columns show All, MC, and SPL, respectively. Curves show saturating exponential fits; black markers and dashed lines indicate performance at the selected population size, and green lines indicate chance accuracy (16.7%).

FIGURE S6

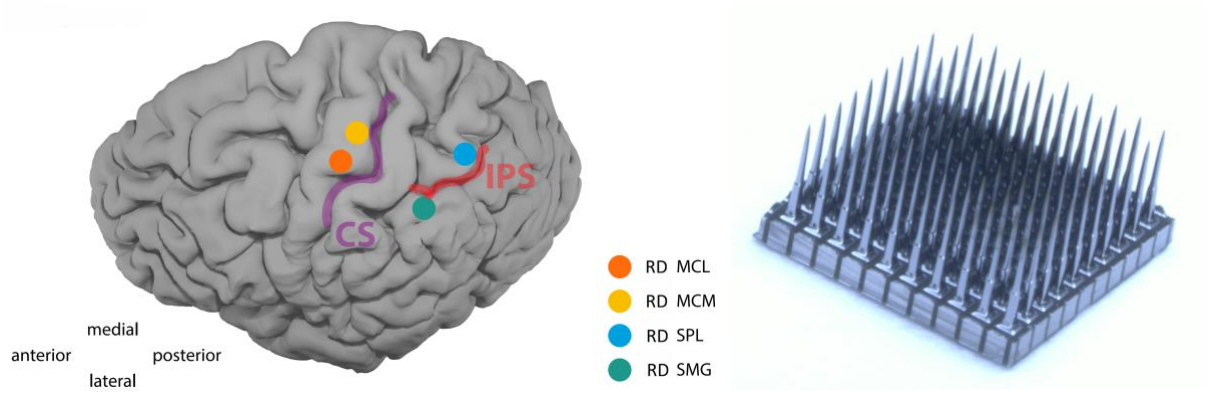


Figure S6: Implant Locations and Neuroport Array.
Anatomical locations of participant RD's implants. Zoomed in photo of the Neuroport Utah electrode array.

FIGURE S7

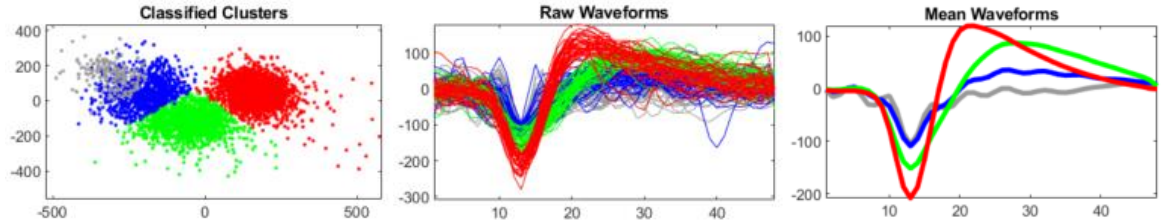


Figure S7: Spike Sorting
Standard output of our spike sorting algorithm. The first plot is a scatter plot of all recorded spikes from a single electrode projected into the first two principal components of waveform space. This example shows three clusters in waveform space corresponding to three unique single units. The second plot shows all recorded spike waveforms color coded by their cluster. The third plot shows the mean waveform of each cluster.